J. Fluid Mech. (2024), *vol*. 1001, A14, doi:10.1017/jfm.2024.1083

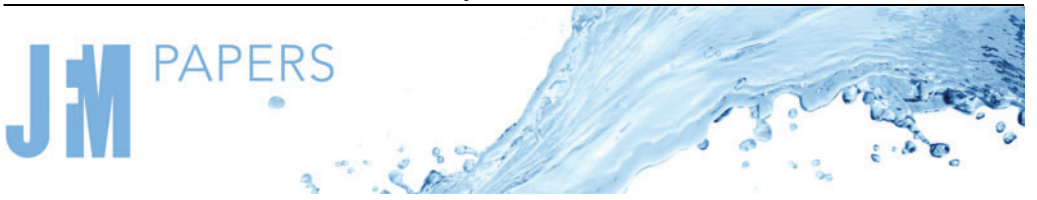

A long-wave model for a falling upper convected Maxwell film inside a tube

Roberto Camassa[1], **H. Reed Ogrosky**[2,†] **and Jeffrey Olander**[1]

[1]Carolina Center for Interdisciplinary Applied Mathematics, Department of Mathematics, University of North Carolina, Chapel Hill, NC 27599-3250, USA

[2]Department of Mathematics and Applied Mathematics, Virginia Commonwealth University, Richmond, VA 23220, USA

(Received 31 May 2024; revised 27 September 2024; accepted 3 November 2024)

A long-wave asymptotic model is developed for a viscoelastic falling film along the inside of a tube; viscoelasticity is incorporated using an upper convected Maxwell model. The dynamics of the resulting model in the inertialess limit is determined by three parameters: Bond number *Bo*, Weissenberg number *We* and a film thickness parameter *a*. The free surface is unstable to long waves due to the Plateau–Rayleigh instability; linear stability analysis of the model equation quantifies the degree to which viscoelasticity increases both the rate and wavenumber of maximum growth of instability. Elasticity also affects the classification of instabilities as absolute or convective, with elasticity promoting absolute instability. Numerical solutions of the nonlinear evolution equation demonstrate that elasticity promotes plug formation by reducing the critical film thickness required for plugs to form. Turning points in travelling wave solution families may be used as a proxy for this critical thickness in the model. By continuation of these turning points, it is demonstrated that in contrast to Newtonian films in the inertialess limit, in which plug formation may be suppressed for a film of any thickness so long as the base flow is strong enough relative to surface tension, elasticity introduces a maximum critical thickness past which plug formation occurs regardless of the base flow strength. Attention is also paid to the trade-off of the competing effects introduced by increasing *We* (which increases growth rate and promotes plug formation) and increasing *Bo* (which decreases growth rate and inhibits plug formation) simultaneously.

Key words: absolute/convective instability, thin films, viscoelasticity

† Email address for correspondence: hrogrosky@vcu.edu

1. Introduction

The flow of highly viscous films along the inside or outside of tubes arises in numerous applications in engineering and the sciences (Oron, Davis & Bankoff 1997; Grotberg & Jensen 2004; Craster & Matar 2009), and many modelling, experimental and computational studies have been conducted to better understand these flows. In contrast to films falling along an inclined plane, in which surface tension acts to stabilize any free-surface instabilities, these flows are unstable to long-wave disturbances as surface tension plays both a stabilizing and destabilizing role due to the curvature of the free surface (see, e.g. Goren 1962; Yih 1967; Hickox 1971). This Plateau–Rayleigh instability is the same mechanism at work in the breakup of liquid jets; depending on the set-up, other instability mechanisms can be at play as well, e.g. the Kapitza instability (Kapitza 1948) which arises due to inertial effects. As the focus of the current study is highly viscous films, the Plateau–Rayleigh instability is primarily in mind here.

Experiments show that there are multiple dynamical outcomes for falling film flows inside a tube. If the film is thinner than some critical thickness, the instability growth will saturate resulting in a free surface consisting of travelling wave trains. However, if the film is thicker than this critical thickness, wave growth can accelerate with the wave crest approaching the centre of the tube in finite time, resulting in the formation of a liquid plug. This critical thickness depends on the strength of the base flow relative to the effects of surface tension (measured by, e.g. the Bond number Bo). The presence of a base flow, here driven by gravity, provides a nonlinearly stabilizing mechanism to halt wave growth; hence the critical thickness is larger with stronger base flow.

Lubrication theory provides a modelling framework to study these flows; a brief review of the modelling studies most closely related to the current set-up is now given. Hammond (1983) derived a thin-film model for the free-surface evolution of a film coating a tube in the absence of any base flow due to gravity or core flow. Frenkel (1992) derived a thin-film model valid for a falling film along the inside or outside of a tube, and numerically studied the free surface evolution and travelling wave solutions (Kerchman & Frenkel 1994). Kalliadasis & Chang (1994) used self-similar solutions to the model of Frenkel (1992) to find an expression for the blow-up of solitary wave solutions which provides a condition for plug or droplet formation. Craster & Matar (2006), Kliakhandler, Davis & Bankoff (2001), Ji *et al.* (2019), Camassa & Lee (2006), Camassa, Ogrosky & Olander (2014) and others all developed what will be termed here as 'long-wave' models for the same set-up, with the first three focused on flow outside of a tube, and the last two focused on flow inside a tube. The designation 'long-wave' is used here to distinguish these models – in which the film is not necessarily assumed to be thin relative to the tube radius – from those in which the thinness of the film is assumed small and directly exploited in the development of the model. A weighted-residual integral boundary-layer (WRIBL) model was developed by Dietze & Ruyer-Quil (2015) for the same set-up, also accounting for the presence of core flow.

The long-wave and WRIBL models have been shown to provide good quantitative agreement with experimental outcomes, with the WRIBL models capable of describing flows with small to moderate Reynolds number particularly well. The linear growth and propagation of free-surface disturbances seen in experiments, as well as the relationship between volume flux and film thickness, has been well captured by both types of models (Smolka, North & Guerra 2008; Camassa *et al.* 2014). When linear stability analysis is conducted from a spatiotemporal viewpoint, instabilities may be classified as absolute or convective (borrowing from the nomenclature of the study of plasmas). Duprat *et al.* (2007) used the model of Craster & Matar (2006) to show that this classification

quantitatively matched experiments on the exterior of a tube in which instability growth was or was not visible near the inlet, respectively; this was subsequently extended for the case of flows along the interior of a tube by Camassa *et al.* (2014). Jensen (2000) studied the conditions under which symmetric unduloids might form plugs. Further studies using long-wave and WRIBL models have highlighted the role gravity plays in breaking wave symmetry and modifying the critical thickness required for plugs to form; numerical simulations of these models predict this critical thickness well (Camassa *et al.* 2014; Dietze, Lavalle & Ruyer-Quil 2020).

This critical thickness is also well captured by families of travelling wave solutions found for long-wave and WRIBL models. Such families, when found for constant values of Bo and varying film thickness, e.g. have a turning point at some thickness, where two branches of travelling wave solution families parametrized by thickness merge; for larger thicknesses, no such solutions are found. This turning-point thickness has been shown to be a good proxy for the critical thickness required for plug formation to occur in both types of models over a variety of parameters (Camassa *et al.* 2014, 2016; Ding *et al.* 2019; Dietze *et al.* 2020; Schwitzerlett, Ogrosky & Topaloglu 2023).

In some applications – e.g. the flow of airway surface liquid lining human airways (Chen *et al.* 2019) – the film is non-Newtonian. A variety of constitutive equations have been proposed to incorporate the effects of elasticity, with two of the simplest and most common being the Oldroyd-B and upper convected Maxwell (UCM) models. The linear stability of a falling viscoelastic film has been studied by Zhou *et al.* (2014), who conducted linear stability analysis of a UCM film in the presence of shear and surfactant. They showed that elasticity is destabilizing for a falling film in the absence of shear, but that elasticity can have a stabilizing or destabilizing effect in the presence of shear. Zhou *et al.* (2016) developed an integral boundary layer model for a viscoelastic film falling down a flexible tube to study the impact of elasticity on the Kapitza and Plateau–Rayleigh instabilities; travelling wave solutions and transient numerical solutions demonstrated the impact elasticity has on wave speed, profile and plug formation. Kang & Chen (1995) developed an asymptotic model for the flow of an Oldroyd-B film down an inclined plane and considered both elastic instability and instability arising from inertia; as with other previous studies, they found that elasticity increases linear instability growth rates, and the weakly nonlinear growth of instabilities was studied. Khayat & Kim (2006) modelled the flow of an Oldroyd-B film flowing over axisymmetric substrates, studying the effects of both inertia and elasticity, and showed the role of viscoelasticity in increasing the accumulation of the film at the inlet. Halpern, Fujioka & Grotberg (2010) developed a lubrication-theory-type model for a viscoelastic film inside a tube in the absence of any base flow, showing that growth rates, plug formation and wall stresses were promoted by elasticity. The impact of elasticity on wall stresses, particularly before and after plug formation or rupture, was further studied numerically by Romano *et al.* (2021), who used an axisymmetric finite volume method to investigate the wall stresses for Oldroyd-B and FENE-CR films; they showed that elasticity results in a second peak in stress gradients arising after plug formation, with this second peak large enough to cause damage to epithelial cells in human airways. Patne (2021) studied the linear stability of a viscoelastic, shear-thinning film over a flexible wall with surfactant at the free surface in the presence of shear from airflow; liquid elastic modes, excited by the first normal stress difference across the free surface, and solid elastic modes, triggered by the shear, can undergo resonance leading to an amplified growth rate. Patne (2024) studied the impacts of air temperature on a UCM film sheared by turbulent airflow inside a tube, demonstrating the stabilizing effects of warm air on free-surface instabilities. The role of viscoelasticity on mucociliary

clearance in lungs has been studied by Choudhury *et al.* (2023), who used the slip model of Bottier *et al.* (2017) and Bottier (2017) to model the beating of cilia on clearance of an Oldroyd-B film and also explored the impact of shear-thinning on mucociliary clearance. The impact of plug formation on mucus clearance and flow resistance in the lungs was studied by Fujioka *et al.* (2016), who developed a semiempirical formula for flow resistance caused by plugs, and Bahrani *et al.* (2022), who considered elastoviscoplastic plugs. Erken *et al.* (2023) incorporated elastoviscoplastic properties of mucus for healthy patients and patients with a variety of airway diseases in an airway closure model. The effect of surfactant on a viscoplastic layer was explored in detail by Shemilt *et al.* (2022, 2023), who showed that both surfactant and yield stress suppress plug formation.

Experimentally, Kim *et al.* (1986) studied air-driven transport of a viscoelastic film up a tube, showing that viscoelasticity greatly reduced the pressure drop across the tube; viscoelasticity was also found to increase the speed of film transport in vertical tubes with (asymmetric) oscillatory airflow (Kim, Iglesias & Sackner 1987) and with constant upward airflow (Kim *et al.* 1986). Boulogne, Pauchard & Giorgiutti-Dauphiné (2012) studied flow on a fibre, showing that a shear-thinning film was thinner than its Newtonian counterpart for fixed volume flux, and that growth rate increased. They also point out that the polymers responsible for non-Newtonian rheology also created an effective surface tension lower than the original. Boulogne *et al.* (2013) discuss how polymers can even suppress the Plateau–Rayleigh instability for viscoelastic films on a fibre. For films inside a tube, experiments by Olander (2020) demonstrated that the addition of a small concentration of polymers may lower the surface tension of a fluid film while producing negligible elastic properties.

In the current study, we develop an asymptotic model for the free-surface evolution of a falling viscoelastic film using a UCM model for the constitutive equations. This model will be used to determine the impact of elasticity on the linear instability of a film, with an analytical expression obtained for the classification of instabilities as absolute or convective. The nonlinear evolution of the free surface will be explored numerically, and travelling wave solution families are explored via numerical continuation of the limit points that serve as proxy for the critical film thickness in model simulations. This continuation succinctly shows the reduction in critical thickness that elasticity induces in the model.

The rest of the paper is organized as follows. The model is developed in § 2, and parameter values corresponding to previous experiments are discussed. Linear stability analysis from both a temporal and spatiotemporal viewpoint is conducted in § 3. Solutions to the model, including those for travelling waves, are found numerically and discussed in § 4. Conclusions are given in § 5.

2. Long-wave model

In this section, a long-wave asymptotic model is derived for a highly viscous viscoelastic falling film coating the interior of a vertical rigid tube.

2.1. *Governing equations and UCM model*

The governing equations are the incompressible, axisymmetric Navier–Stokes equations in cylindrical coordinates,

$$\bar{\rho}(\partial_{\bar{t}}\bar{u} + \bar{u}\partial_{\bar{r}}\bar{u} + \bar{w}\partial_{\bar{z}}\bar{u}) = -\partial_{\bar{r}}\bar{p} + \frac{1}{\bar{r}}\partial_{\bar{r}}(\bar{r}\bar{\sigma}_{rr}) + \partial_{\bar{z}}\bar{\sigma}_{rz} - \frac{\bar{\sigma}_{\theta\theta}}{\bar{r}}, \tag{2.1a}$$

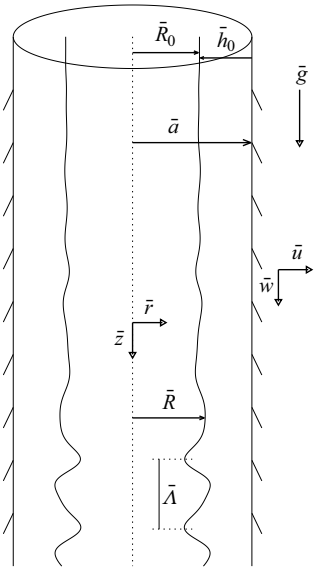

Figure 1. Sketch of the flow configuration and variable definitions.

$$\bar{\rho}(\partial_{\bar{t}}\bar{w} + \bar{u}\partial_{\bar{r}}\bar{w} + \bar{w}\partial_{\bar{z}}\bar{w}) = -\partial_{\bar{z}}\bar{p} + \frac{1}{\bar{r}}\partial_{\bar{r}}(\bar{r}\bar{\sigma}_{rz}) + \partial_{\bar{z}}\bar{\sigma}_{zz} + \bar{\rho}\bar{g}, \tag{2.1b}$$

$$\frac{1}{\bar{r}}\partial_{\bar{r}}(\bar{r}\bar{u}) + \partial_{\bar{z}}\bar{w} = 0, \tag{2.1c}$$

where $\bar{\rho}$ is the density of the fluid, $\bar{g}$ is acceleration due to gravity, $\bar{p}$ is pressure, $\bar{t}$ is time, and $\bar{\sigma}$ is the deviatoric stress tensor with components $\bar{\sigma}_{rr}$, $\bar{\sigma}_{rz}$ and $\bar{\sigma}_{zz}$. Overbars denote dimensional quantities and partial derivatives with respect to, e.g. $\bar{r}$, are denoted $\partial_{\bar{r}}$. The coordinates are $(\bar{r}, \bar{\theta}, \bar{z})$ with associated velocity components $(\bar{u}, \bar{v}, \bar{w})$; see figure 1. Here, the axial coordinate $\bar{z}$ increases in the downward direction along the tube. The flow is assumed to be axisymmetric, so the $\bar{\theta}$ and $\bar{v}$ components are taken to be zero.

A model for the deviatoric stress components is needed to close the system. Many models have been proposed and seen widespread use; here, we choose to use the UCM model. Under the UCM model, each of the stress components $\bar{\sigma}_{ij}$ are assumed to obey the following constitutive equations:

$$\bar{\sigma}_{rr} + \bar{\lambda}[\partial_{\bar{t}}\bar{\sigma}_{rr} + \bar{u}\partial_{\bar{r}}\bar{\sigma}_{rr} + \bar{w}\partial_{\bar{z}}\bar{\sigma}_{rr} - 2(\partial_{\bar{r}}\bar{u})\bar{\sigma}_{rr} - 2(\partial_{\bar{z}}\bar{u})\bar{\sigma}_{rz}] = 2\bar{\mu}\partial_{\bar{r}}\bar{u}, \tag{2.2a}$$

$$\begin{aligned}\bar{\sigma}_{rz} + \bar{\lambda}[&\partial_{\bar{t}}\bar{\sigma}_{rz} + \bar{u}\partial_{\bar{r}}\bar{\sigma}_{rz} + \bar{w}\partial_{\bar{z}}\bar{\sigma}_{rz} - (\partial_{\bar{r}}\bar{w})\bar{\sigma}_{rr} - (\partial_{\bar{r}}\bar{u} + \partial_{\bar{z}}\bar{w})\bar{\sigma}_{rz} - (\partial_{\bar{z}}\bar{u})\bar{\sigma}_{zz}] \\ &= \bar{\mu}(\partial_{\bar{z}}\bar{u} + \partial_{\bar{r}}\bar{w}),\end{aligned} \tag{2.2b}$$

$$\bar{\sigma}_{zz} + \bar{\lambda}[\partial_{\bar{t}}\bar{\sigma}_{zz} + \bar{u}\partial_{\bar{r}}\bar{\sigma}_{zz} + \bar{w}\partial_{\bar{z}}\bar{\sigma}_{zz} - 2(\partial_{\bar{r}}\bar{w})\bar{\sigma}_{rz} - 2(\partial_{\bar{z}}\bar{w})\bar{\sigma}_{zz}] = 2\bar{\mu}\partial_{\bar{z}}\bar{w}, \tag{2.2c}$$

$$\bar{\sigma}_{\theta\theta} + \bar{\lambda}[\partial_{\bar{t}}\bar{\sigma}_{\theta\theta} + \bar{u}\partial_{\bar{r}}\bar{\sigma}_{\theta\theta} + \bar{w}\partial_{\bar{z}}\bar{\sigma}_{\theta\theta}] = \frac{2\bar{\mu}\bar{u}}{\bar{r}}, \tag{2.2d}$$

where $\bar{\lambda}$ is the relaxation time, $\bar{\mu}$ is the dynamic viscosity and where the right-hand side of (2.2) are the components of the rate-of-strain tensor $\bar{\tau}$.

Boundary conditions at the tube wall, $\bar{r} = \bar{a}$, are no-slip,

$$\bar{u} = \bar{w} = 0. \tag{2.3}$$

At the free surface, $\bar{r} = \bar{R}(\bar{z}, \bar{t})$, the boundary conditions are given by: (i) continuity of tangential stress; (ii) jump in normal stress according to the Young–Laplace equation; and (iii) a kinematic boundary condition,

$$\bar{\sigma}_{rz} + (\partial_{\bar{z}}\bar{R})(\bar{\sigma}_{rr} - \bar{\sigma}_{zz}) - (\partial_{\bar{z}}\bar{R})^2\bar{\sigma}_{rz} = 0, \tag{2.4a}$$

$$-\bar{p}[1 + (\partial_{\bar{z}}\bar{R})^2] + \bar{\sigma}_{rr} - 2(\partial_{\bar{z}}\bar{R})\bar{\sigma}_{rz} + (\partial_{\bar{z}}\bar{R})^2\bar{\sigma}_{zz} = \bar{\gamma}[1 + (\partial_{\bar{z}}\bar{R})^2]\left(\frac{1}{\bar{R}[1 + (\partial_{\bar{z}}\bar{R})^2]^{1/2}} - \frac{\partial_{\bar{z}\bar{z}}\bar{R}}{[1 + (\partial_{\bar{z}}\bar{R})^2]^{3/2}}\right), \tag{2.4b}$$

$$\bar{u} = \partial_{\bar{t}}\bar{R} + \bar{w}\partial_{\bar{z}}\bar{R}, \tag{2.4c}$$

where the background pressure has been set to zero for convenience.

Equations (2.1)–(2.4) may be non-dimensionalized by the scales

$$r = \frac{\bar{r}}{\bar{R}_0}, \quad z = \frac{\bar{z}}{\bar{\Lambda}}, \quad u = \frac{\bar{u}}{\bar{U}_0}, \quad w = \frac{\bar{w}}{\bar{W}_0}, \quad t = \frac{\bar{t}\bar{W}_0}{\bar{\Lambda}}, \quad p = \frac{\bar{p}}{\bar{\rho}\bar{g}\bar{R}_0}, \quad \sigma_{ij} = \frac{\bar{\sigma}_{ij}}{\bar{\rho}\bar{g}\bar{R}_0}, \tag{2.5a–g}$$

where $\bar{R}_0 = \bar{a} - \bar{h}_0$ is the distance from the centre of the tube to the mean free surface of the film, $\bar{\Lambda}$ is a typical wavelength of a free-surface disturbance, and where $\bar{U}_0$ and $\bar{W}_0 = \bar{\rho}\bar{g}\bar{R}_0^2/\bar{\mu}$ are velocity scales in the radial and axial directions, respectively. The model development that follows will make use of a long-wave assumption that exploits an assumed small ratio of length scales $\epsilon = \bar{R}_0/\bar{\Lambda} \ll 1$. The continuity equation then dictates that $\bar{U}_0 = \epsilon\bar{W}_0$. This results in the following dimensionless governing equations:

$$\epsilon^2\widetilde{Re}(\partial_t u + u\partial_r u + w\partial_z u) = -\partial_r p + \frac{1}{r}\partial_r(r\sigma_{rr}) + \epsilon\partial_z\sigma_{rz} - \frac{\sigma_{\theta\theta}}{r}, \tag{2.6a}$$

$$\epsilon\widetilde{Re}(\partial_t w + u\partial_r w + w\partial_z w) = -\epsilon\partial_z p + \frac{1}{r}\partial_r(r\sigma_{rz}) + \epsilon\partial_z\sigma_{zz} + 1, \tag{2.6b}$$

$$\frac{1}{r}\partial_r(ru) + \partial_z w = 0, \tag{2.6c}$$

where $\widetilde{Re} = \bar{\rho}\bar{R}_0\bar{W}_0/\bar{\mu}$ is the Reynolds number. In dimensionless form, the constitutive equations are

$$\sigma_{rr} + \epsilon\widetilde{We}[\partial_t\sigma_{rr} + u\partial_r\sigma_{rr} + w\partial_z\sigma_{rr} - 2(\partial_r u)\sigma_{rr} - 2\epsilon(\partial_z u)\sigma_{rz}] = 2\epsilon\partial_r u, \tag{2.7a}$$

$$\sigma_{rz} + \widetilde{We}[\epsilon\partial_t\sigma_{rz} + \epsilon u\partial_r\sigma_{rz} + \epsilon w\partial_z\sigma_{rz} - (\partial_r w)\sigma_{rr} - \epsilon(\partial_r u + \partial_z w)\sigma_{rz} - \epsilon^2(\partial_z u)\sigma_{zz}] = \epsilon^2\partial_z u + \partial_r w, \tag{2.7b}$$

$$\sigma_{zz} + \widetilde{We}[\epsilon\partial_t\sigma_{zz} + \epsilon u\partial_r\sigma_{zz} + \epsilon w\partial_z\sigma_{zz} - 2(\partial_r w)\sigma_{rz} - 2\epsilon(\partial_z w)\sigma_{zz}] = 2\epsilon\partial_z w, \tag{2.7c}$$

$$\sigma_{\theta\theta} + \epsilon\widetilde{We}[\partial_t\sigma_{\theta\theta} + u\partial_r\sigma_{\theta\theta} + w\partial_z\sigma_{\theta\theta}] = \frac{2\epsilon u}{r}, \tag{2.7d}$$

where $\widetilde{We} = \bar{\lambda}\bar{W}_0/\bar{R}_0$ is the Weissenberg number, the value of which specifies the ratio of elastic forces to viscous forces in the problem. Boundary conditions at the tube wall,

$r = a$, where $a = \bar{a}/\bar{R}_0$, are

$$u = w = 0, \tag{2.8}$$

and at the free surface, $r = R(z, t)$,

$$[1 - \epsilon^2(\partial_z R)^2]\sigma_{rz} + \epsilon(\partial_z R)(\sigma_{rr} - \sigma_{zz}) = 0, \tag{2.9a}$$

$$\begin{aligned} &-p[1 + \epsilon^2(\partial_z R)^2] + \sigma_{rr} - 2\epsilon(\partial_z R)\sigma_{rz} + \epsilon^2(\partial_z R)^2\sigma_{zz} \\ &\quad = \frac{1}{\widetilde{Bo}}[1 + \epsilon^2(\partial_z R)^2]\left(\frac{1}{R[1 + \epsilon^2(\partial_z R)^2]^{1/2}} - \frac{\epsilon^2\partial_{zz}R}{[1 + \epsilon^2(\partial_z R)^2]^{3/2}}\right), \end{aligned} \tag{2.9b}$$

$$u = \partial_t R + w\partial_z R, \tag{2.9c}$$

where $\widetilde{Bo} = \bar{\rho}\bar{g}\bar{R}_0^2/\bar{\gamma}$ is the Bond number, whose value specifies the ratio of gravity forces to capillary forces. We thus have a total of five dimensionless parameters governing the flow: film thickness parameter a, Reynolds number $\widetilde{Re}$, Bond number $\widetilde{Bo}$, Weissenberg number $\widetilde{We}$ and aspect ratio ϵ.

2.2. *Leading-order equations and solution*

Integrating the continuity equation (2.6*c*) across the fluid layer and applying the boundary conditions (2.8) and (2.9*c*) results in an evolution equation for the free surface $R(z, t)$,

$$\partial_t R = \frac{1}{R}\partial_z \int_R^a wr\,\mathrm{d}r. \tag{2.10}$$

All that is needed to close the model is an expression for the axial velocity w. To find an approximation of w, a regular perturbation expansion in ϵ is used, with each variable expressed as

$$w = w_0 + \epsilon w_1 + O(\epsilon^2), \quad p = p_0 + \epsilon p_1 + O(\epsilon^2), \tag{2.11a}$$

$$u = u_0 + \epsilon u_1 + O(\epsilon^2), \quad \sigma_{ij} = \sigma_{ij,0} + \epsilon\sigma_{ij,1} + O(\epsilon^2). \tag{2.11b}$$

Substituting (2.11) into the governing equations (2.6) and truncating at leading order in ϵ results in

$$\partial_r p_0 = \frac{1}{r}\partial_r(r\sigma_{rr,0}) - \frac{\sigma_{\theta\theta,0}}{r}, \quad \frac{1}{r}\partial_r(r\sigma_{rz,0}) = -1, \quad \frac{1}{r}\partial_r(ru_0) + \partial_z w_0 = 0, \tag{2.12a–c}$$

and the constitutive equations of the UCM model are given by

$$\sigma_{rr,0} = 0, \tag{2.13a}$$

$$\sigma_{rz,0} - \widetilde{We}(\partial_r w_0)\sigma_{rr,0} = \partial_r w_0, \tag{2.13b}$$

$$\sigma_{zz,0} - 2\widetilde{We}(\partial_r w_0)\sigma_{rz,0} = 0, \tag{2.13c}$$

$$\sigma_{\theta\theta,0} = 0. \tag{2.13d}$$

The no-slip boundary condition at $r = a$ dictates $u_0 = w_0 = 0$, and at $r = R(z, t)$, the boundary conditions are

$$\sigma_{rz} = 0, \quad -p_0 + \sigma_{rr,0} = \frac{1}{\widetilde{Bo}}\left(\frac{1}{R} - \epsilon^2 R_{zz}\right), \tag{2.14}$$

where we have retained one term of higher order in ϵ. While a full discussion of the retention of this term is omitted here, this term is commonly included in long-wave

asymptotic models and has been shown to be the first-appearing term in the expansion that prevents shock formation; it also provides the correct cut-off wavenumber for linearly unstable modes and produces excellent agreement with experiments for Newtonian films.

The leading-order solution to (2.12*a–c*)–(2.14) is given by

$$\left.\begin{aligned} u_0 &= \frac{R(\partial_z R)}{4r}\left(r^2 - a^2 - 2r^2\log\frac{r}{a}\right), \quad \sigma_{rz,0} = \frac{1}{2r}(R^2 - r^2), \\ w_0 &= \frac{1}{4}\left(a^2 - r^2 + 2R^2\log\frac{r}{a}\right), \quad \sigma_{zz,0} = \frac{\widetilde{We}}{2r^2}(R^2 - r^2)^2, \\ p_0 &= -\frac{1}{\widetilde{Bo}}\left(\frac{1}{R} - \epsilon^2\partial_{zz}R\right), \quad \sigma_{rr,0} = \sigma_{\theta\theta,0} = 0. \end{aligned}\right\} \tag{2.15}$$

Note that the presence of elasticity does not modify the leading order base flow (u, w), but does modify the $\sigma_{zz,0}$ component of the stress tensor. Equation (2.15) results in a leading-order model

$$\partial_t R = \frac{1}{R}\partial_z\int_R^a w_0 r\,\mathrm{d}r = \frac{1}{2}\left(R^2 - a^2 - 2R^2\log\frac{R}{a}\right)\partial_z R. \tag{2.16}$$

2.3. *First-order equations and long-wave model*

Next, the base flow may be used to find the first-order axial velocity w_1. The case of low-Reynolds-number flow, i.e. $\widetilde{Re} = O(\epsilon)$, is considered first. In this case, the inertial terms appear at $O(\epsilon^2)$ and the governing equations at first-order in ϵ are given by

$$\partial_r p_1 = \frac{1}{r}\partial_r(r\sigma_{rr,1}) + \partial_z\sigma_{rz,0} - \frac{\sigma_{\theta\theta,1}}{r}, \tag{2.17a}$$

$$\frac{1}{r}\partial_r(r\sigma_{rz,1}) = \partial_z p_0 - \partial_z\sigma_{zz,0}, \tag{2.17b}$$

$$\frac{1}{r}\partial_r(ru_1) + \partial_z w_1 = 0. \tag{2.17c}$$

The UCM model constitutive equations are

$$\sigma_{rr,1} = 2\partial_r u_0, \tag{2.18a}$$

$$\begin{aligned} &\sigma_{rz,1} + \widetilde{We}[\partial_t\sigma_{rz,0} + u_0\partial_r\sigma_{rz,0} + w_0\partial_z\sigma_{rz,0} \\ &\quad -(\partial_r w_0)\sigma_{rr,1} - (\partial_r w_1)\sigma_{rr,0} - (\partial_r u_0 + \partial_z w_0)\sigma_{rz,0}] = \partial_r w_1, \end{aligned} \tag{2.18b}$$

$$\begin{aligned} &\sigma_{zz,1} + \widetilde{We}[\partial_t\sigma_{zz,0} + u_0\partial_r\sigma_{zz,0} + w_0\partial_z\sigma_{zz,0} \\ &\quad -2(\partial_r w_0)\sigma_{rz,1} - 2(\partial_r w_1)\sigma_{rz,0} - 2(\partial_z w_0)\sigma_{zz,0}] = 2\partial_z w_0, \end{aligned} \tag{2.18c}$$

$$\sigma_{\theta\theta,1} = \frac{2u_0}{r}. \tag{2.18d}$$

Once again, no-slip boundary conditions apply at the wall $r = a$, while at the free surface $r = R(z, t)$, the first-order boundary conditions are

$$\sigma_{rz,1} + (\partial_z R)(\sigma_{rr,0} - \sigma_{zz,0}) = 0, \tag{2.19a}$$

$$-p_1 + \sigma_{rr,1} - 2(\partial_z R)\sigma_{rz,0} = 0. \tag{2.19b}$$

While each equation and condition has been given through first-order, only (2.17*b*), (2.18*a*), (2.18*b*) and (2.19*a*) are needed to derive the first-order axial velocity w_1. In solving for w_1,

note that (2.18*b*) contains $\partial_t \sigma_{rz,0} = RR_t/r$; to evaluate this contribution from the leading order stress, we use the leading order model (2.16) to substitute for $\partial_t R$. This approach is identical to that taken by e.g. Camassa *et al.* (2014) to incorporate inertial effects. Note that this approach may not be applicable to settings without a base flow, as considered by Halpern *et al.* (2010), for example. This results in the following expression for w_1:

$$w_1 = \frac{1}{4\widetilde{Bo}}\left(r^2 - a^2 - 2R^2\log\frac{r}{a}\right)\left(\frac{\partial_z R}{R^2} + \partial_{zzz}R\right) + \frac{\widetilde{We}R(\partial_z R)}{8}\left[r^2 - a^2 - R^2 + \frac{a^2R^2}{r^2} + 2(a^2 - R^2)\log\frac{r}{a} + 4R^2\log\frac{r}{a}\left(\log\frac{R}{a} + \log\frac{R}{r}\right)\right]. \tag{2.20}$$

Using (2.15) and substituting $w_0 + \epsilon w_1$ into (2.10), the model equation is

$$\partial_t R = \frac{1}{16R}\partial_z\left[f_1(R;a)\left(1 - \frac{a^2}{Bo}\left(\frac{\partial_z R}{R^2} + \partial_{zzz}R\right)\right) - \frac{WeR(\partial_z R)}{2a}f_2(R;a)\right], \tag{2.21}$$

where

$$f_1(R;a) = a^4 - 4a^2R^2 + 3R^4 - 4R^4\log\frac{R}{a}, \tag{2.22a}$$

$$f_2(R;a) = 3a^4 - 3R^4 - 4R^4\log\frac{R}{a} + 16a^2R^2\log\frac{R}{a} + 8R^4\left(\log\frac{R}{a}\right)^2, \tag{2.22b}$$

and where we have dropped the ϵ's from the final model equation. This corresponds to returning to the original aspect ratio in the dimensionless problem; while the ϵ's are no longer in the model equation, it must be pointed out that the strict validity of the model derivation still relies on the assumption $\epsilon \ll 1$ is satisfied. Note that (2.21) has been expressed in terms of a rescaled Bond number $Bo = a^2\widetilde{Bo}$ and Weissenberg number $We = a\widetilde{We}$; these rescaled numbers $Bo = \bar{\rho}\bar{g}\bar{a}^2/\bar{\gamma}$ and $We = \bar{\lambda}\bar{\rho}\bar{g}\bar{a}/\bar{\mu}$ have the advantage of being independent of film thickness and depend only on parameters density, viscosity, tube radius, surface tension and relaxation time. It is interesting to note that the same model equation may be derived using the Oldroyd-B constitutive equations in place of the UCM model, so that the dynamical outcomes produced by either constitutive model are identical. Note that $f_i(R;a) > 0$ (for $i = 1, 2$) since $0 < R < a$.

In the case where $Re = O(1)$, the inertial terms appear at first-order; the details of the derivation in the case of a Newtonian film can be found from Camassa *et al.* (2014) and are omitted here as the resulting terms are identical (up to choice of scales):

$$\partial_t R = \frac{1}{16R}\partial_z\left[f_1(R;a)\left(1 - \frac{a^2}{Bo}\left(\frac{\partial_z R}{R^2} + \partial_{zzz}R\right)\right) - \frac{WeR(\partial_z R)}{2a}f_2(R;a) - \frac{Re}{a^3}f_3(R;a)\partial_z R\right], \tag{2.23}$$

where

$$f_3(R;a) = \tfrac{59}{48}R^7 - \tfrac{15}{16}a^2R^5 - \tfrac{9}{16}a^4R^3 + \tfrac{13}{48}a^6R - \tfrac{17}{4}a^2R^5\log(R/a) + \tfrac{7}{4}a^4R^3\log(R/a) - \tfrac{5}{2}R^7(\log(R/a))^2 + \tfrac{5}{2}a^2R^5(\log(R/a))^2 + 2R^7(\log(R/a))^3, \tag{2.24}$$

and where $Re = a^3\widetilde{Re} = \bar{\rho}^2\bar{g}\bar{a}^3/\bar{\mu}^2$ is a rescaled Reynolds number. As the focus here is on highly viscous films, model results will be primarily presented for (2.21), but comments will be given on (2.23) as well. It is again the case that $f_3(R; a) > 0$ for $0 < R < a$.

In the thin-film limit, the nonlinearities in the model simplify considerably. A film thickness h, scaled so that $h = 0$ at the wall and $h = 1$ at the mean free surface, may be defined by

$$h = \frac{a - R}{a - 1}. \tag{2.25}$$

Substituting $R = a - \beta h$, with $\beta = a - 1$, into (2.21) and expanding about $\beta = 0$ results in

$$\partial_t h + \frac{1}{3}\partial_z\left[h^3\left(1 + \frac{1}{Bo^*}(\partial_z h + \partial_{zzz} h)\right) + We^* h^4(\partial_z h)\right] = 0, \tag{2.26}$$

where $Bo^* = Bo/\beta$, $We^* = \beta^2 We$ and where time has been rescaled by β^2. Equation (2.26) is similar to that of Frenkel (1992) but with viscoelasticity included, and is also similar to that of Kang & Chen (1995) for flow down an inclined plane but includes the effects of azimuthal curvature. Note that the viscoelastic term is proportional to h^4, while surface tension and advection terms contain h^3. In that respect – having a higher-order term that will be shown to drive instability growth – it bears some resemblance to the equation derived by Benney (1966) for film flow down an inclined plane, in which instability growth is provided by an inertial term proportional to h^6. For certain parameter values, unbounded solutions to this Benney equation can arise, which has no physical relevance for the falling-film-down-plane problem; this issue can be addressed through use of the WRIBL modelling approach (see, e.g. Ruyer-Quil & Manneville 1998; Dietze & Ruyer-Quil 2015). It would be interesting to conduct a detailed study of (2.26) for similar features, especially since unbounded solutions are not necessarily physically irrelevant given the potential for plug formation in the tube problem considered here, but nonlinear results will be presented here strictly for the model (2.21).

2.4. *Parameter values*

Before presenting model results, a brief discussion is given concerning the range of parameter values for *Bo*, *Re*, *We* and *a* that are in mind here. As the model is derived to consider highly viscous flows, we briefly consider some experimental set-ups for which this model could apply.

In the Newtonian experiments of Camassa *et al.* (2014), a highly viscous silicone oil is used as the solvent, with density, dynamic viscosity and surface tension given approximately by

$$\bar{\rho} = 0.97\,\mathrm{g\,cm^{-3}}, \quad \bar{\mu} = 125\,\mathrm{P}, \quad \bar{\sigma} = 21.5\,\mathrm{dyn\,cm^{-1}}, \tag{2.27a–c}$$

respectively. The inner radius $\bar{a}$ of the tube in the experiments ranged from 0.5 cm down to 0.17 cm; the thickness of the film $\bar{h}_0$ in viscous gravity-driven experiments varied, but most experiments had film thicknesses between 0.1 and 0.2 cm. Using these values results in the following estimated ranges for the dimensionless parameters in the model for a Newtonian fluid,

$$Bo = 1.3 - 11.1, \quad Re = 3 \times 10^{-4} - 7 \times 10^{-3}, \quad a = 1.25 - 2.5. \tag{2.28a–c}$$

As $Re < 0.01$ for all these cases, the focus will primarily be on the inertialess model (2.21), with values of Bond number primarily lying in the range $0.5 < Bo < 15$ and tube radius

parameter $1 < a < 3$, occasionally showing results for other values of Bo or a to illustrate a point about the model.

For viscoelastic films, Shaqfeh, Larson & Frederickson (1989) (see also Kang & Chen 1995) found that the Oldroyd-B model is capable of capturing the behaviour of polymeric thin films so long as $We < 2.5$. Based on this criteria, and given that the model equation here is identical to that obtained using the Oldroyd-B equations, we will largely restrict results to $We < 2.5$.

The addition of polymers to a Newtonian fluid may also modify the surface tension; e.g. an increase in We may in some cases be accompanied by a corresponding increase in Bo. This effect was seen, e.g. in experiments conducted by Olander (2020), in which the falling film consisted of polybutene (PB) and various small concentrations of polyisobutylene (PIB); the PIB concentrations were small enough to result in negligible values of We but still lower the value of Bo through reduction of the surface tension. Some attention will thus be given to the increase in Bo required to offset a given increase in We to produce an equivalent dynamical outcome.

One of the motivations for the experimental values chosen by Camassa *et al.* (2014) was the study of mucus lining human airways; the viscosities, surface tension and tube radii (and hence Bo) were chosen to be representative of upper airways. The rheological properties of human mucus can vary widely with patient, disease and airway generation, with elasticity decreasing with airway generation and increasing in the presence of airway diseases like cystic fibrosis (Lai *et al.* 2009).

3. Linear stability analysis

It is well known that the free surface of a film coating the interior or exterior of a tube is unstable to long-wave disturbances due to the Plateau–Rayleigh instability. The impact of viscoelasticity on this instability is explored next from both a temporal and spatiotemporal viewpoint, with the latter allowing classification of instabilities as convective or absolute.

3.1. *Temporal linear stability analysis*

To study the linear stability of a flat-interface solution $R(z, t) = 1$, let the free surface be perturbed by a superposition of small-amplitude Fourier modes,

$$R = 1 + \hat{R}\exp(\mathrm{i}(kz - \omega t)), \tag{3.1}$$

where k is a spatial wavenumber and where it is assumed that $\hat{R} \ll 1$; while exploring the temporal stability of the free surface, the wavenumber k will be taken to be real-valued. Substituting (3.1) into (2.21) results in the dispersion relation

$$\omega = \frac{k}{2}(a^2 - 1 - 2\log a) + \frac{\mathrm{i}a^2}{16Bo}(k^2 - k^4)f_1(1; a) + \frac{\mathrm{i}We\,k^2}{32a}f_2(1; a). \tag{3.2}$$

The real part of (3.2), $\mathrm{Re}[\omega]/k$, determines the phase speed of disturbances, while the imaginary part, $\mathrm{Im}[\omega]$, dictates the growth of their amplitude. As with other thin-film models, the dispersion relation is similar to that of the Kuramoto–Sivashinsky (KS) equation in the dependence on wavenumber k. For reference, the dispersion relation for the model with inertial terms (2.23) and for the inertialess thin-film model (2.26) are also

included:

$$\omega = \frac{k}{2}(a^2 - 1 - 2\log a) + \frac{\mathrm{i}a^2}{16Bo}(k^2 - k^4)f_1(1;a) + \frac{\mathrm{i}We\,k^2}{32a}f_2(1;a) + \frac{\mathrm{i}Rek^2}{16a^3}f_3(1;a) \tag{3.3}$$

and

$$\omega = \frac{1}{3}\left(k + \frac{\mathrm{i}\beta}{Bo}(k^2 - k^4) + \mathrm{i}We\beta^2k^2\right), \tag{3.4}$$

respectively.

Equation (3.2) has been well studied for Newtonian films ($We = 0$); similar to other settings where the Plateau–Rayleigh instability is the dominant one, the film is unstable to long-wave disturbances with cut-off wavenumber $k_c = 1$ and the wavenumber of maximum growth rate, $k_{max} = 1/\sqrt{2}$, set by a balance of destabilization of the free surface due to its azimuthal curvature and stabilization due to its axial curvature, both arising due to surface tension. The phase speed of disturbances is set by the balance of gravity and viscous forces. In the linear regime, the dimensionless growth rates of this model are determined by the k^2 and k^4 terms arising due to the Plateau–Rayleigh instability, with the growth rates increasing monotonically with a and with $1/Bo$. The inclusion of base flow due to gravity in this first-order model does not impact these dimensionless growth rates as the hyperbolic terms in (2.21) associated with the effects of gravity arise solely in the real part of the dispersion relation, similar to many other first-order film flow models with base flow. This model dispersion relation has been shown to agree well with that of the Stokes equations (Camassa *et al.* 2014).

In the case where $We > 0$, the presence of elasticity introduces a second mechanism of free-surface destabilization. Figure 2(a) shows the growth rates $\mathrm{Im}[\omega(k)]$ (3.2) for $a = 1.4$, $Bo = 1$ and a variety of We values; the growth rate increases with increasing We for all wavenumbers k. The k^2 terms of (3.2) are identical to those of Zhou *et al.* (2014) in their long-wave analysis without surfactant. Both the wavenumber k_{max} of maximum growth rate and the cutoff wavenumber k_c increase as well, according to

$$k_c = \sqrt{1 + \frac{We\,Bo\,f_2(1;a)}{2a^3 f_1(1;a)}}, \quad k_{max} = k_c/\sqrt{2}, \tag{3.5a,b}$$

so that the product $Bo\,We = \bar{\lambda}\bar{\rho}^2\bar{g}^2\bar{a}^3/\bar{\mu}\bar{\gamma}$ determines the change in k_{max} and k_c for fixed a. Figure 2(b) shows this dependence of k_c and k_{max} on We for $a = 1.4$. As the value of Bo increases, changing We results in a larger change in k_{max}.

As with the Newtonian film, the growth rates increase with a and $1/Bo$, but the relative impact of increasing We depends non-monotonically on film thickness parameter a. Figure 2(c) shows the growth rates for a much thinner film with $a = 1.05$. As may be expected, the growth rates are smaller than for $a = 1.4$, but it is also true that the growth rate curves are closer together than in figure 2(a), indicating that increasing We has a smaller relative impact on the growth rates and on k_{max} when $a = 1.05$ than when $a = 1.4$. This may be anticipated from (3.5a,b) or from the thin-film dispersion relation (3.4) in which the term proportional to We occurs at higher order in β than the other terms.

For moderate values of a, the impact of a on k_{max} must be assessed by examining $f_2(1;a)/[a^3 f(1;a)]$ in (3.5a,b); this quantity is plotted in figure 2(d). This value reaches a maximum at $a \approx 1.375$; i.e. this value of a produces the largest impact on k_{max} and largest relative impact on the maximum growth rate GR_{max} for small We as determined by

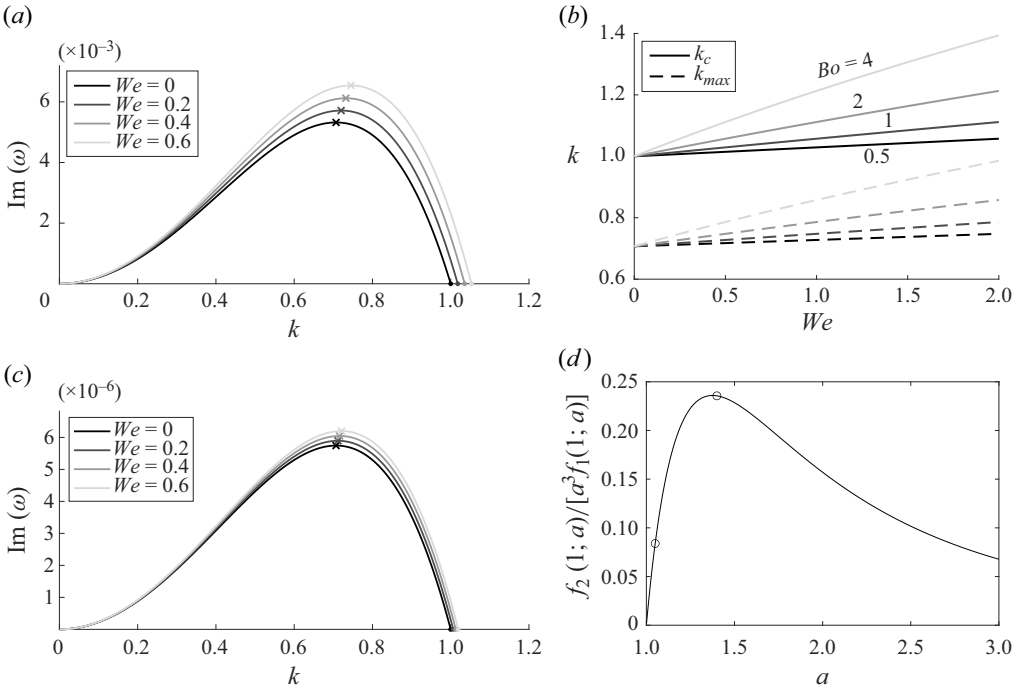

Figure 2. (*a*) Growth rates of (2.21) for $a = 1.4$, $Bo = 2$ and various values of We. Here, $\times$ symbols denote the maximum growth rate GR_{max} and $\cdot$ symbols denote cutoff wavenumber k_c. (*b*) k_{max} and k_c for $a = 1.4$ and various values of Bo and We. (*c*) Same as panel (*a*) but with $a = 1.05$. (*d*) $f_2(1; a)/[a^3 f_1(1; a)]$; maximum value obtained at $a \approx 1.375$. Open circles denote a values used in panels (*a*,*c*).

$[(\partial GR_{max}/\partial We)/GR_{max}]|_{We=0} = f_2(1; a)Bo/[a^3 f_1(1; a)]$. We also note that for thick films (large a), the relative impact of viscoelasticity on k_{max} and growth rates is again small, as $f_2(1; a)/[a^3 f_1(1; a)]$ behaves like $1/a^3$ for large a.

In summary, linear instability is driven by both surface tension and viscoelasticity. While growth rates increase monotonically with a and $1/Bo$, the relative impact of viscoelasticity on growth rates is highest for moderately thick films.

Note that while the base flow w_0 is unchanged by the presence of viscoelasticity, the normal stress is positive, $\sigma_{zz,0} > 0$. This stress term plays a crucial role in determining the sign of the first-order velocity w_1 through (2.17*b*); w_1 may be expressed as the sum of three parts:

$$w_1 = w_{ST} + w_{NS} + w_{UCM}, \tag{3.6}$$

where

$$w_{1,ST} = \frac{1}{4\widetilde{Bo}}\left(r^2 - a^2 - 2R^2 \log\frac{r}{a}\right)\left(\frac{\partial_z R}{R^2} + \partial_{zzz} R\right), \tag{3.7a}$$

$$w_{1,NS} = \frac{\widetilde{We} R R_z}{2}\left(r^2 - a^2 + 2R^2 \log\frac{a}{r}\left(1 + \log\frac{a}{R} + \log\frac{r}{R}\right)\right), \tag{3.7b}$$

$$w_{1,UCM} = \frac{\widetilde{We} R R_z}{8}\left(3a^2 - 3r^2 - R^2 + \frac{a^2 R^2}{r^2} + 6R^2 \log\frac{r}{a} + 2a^2 \log\frac{r}{a} - 4R^2 \log\frac{r}{a}\left(\log\frac{R}{a} + \log\frac{R}{r}\right)\right), \tag{3.7c}$$

where *ST* denotes surface tension, *NS* denotes normal stress corresponding to $\sigma_{zz,0}$ and *UCM* refers to the contribution of the terms in brackets in (2.18*b*). For $R < r < a$, note that if $R_z > 0$, then $w_{1,NS} < 0$, $w_{1,UCM} > 0$ and $w_{1,NS} + w_{1,UCM} < 0$. As a result, the normal stresses (specifically the gradient $\partial_z \sigma_{zz,0}$) generated by the base flow are responsible for the instability growth seen in the current model.

3.2. *Absolute and convective instability*

Linear stability analysis may also be conducted from a spatio-temporal viewpoint, which allows classification of instabilities as absolute or convective. In experiments, convectively unstable films are those in which visible instability growth is only evident downstream, far from the inlet, while absolutely unstable films exhibit visible instability growth right at or near the inlet.

Deissler, Oron & Lee (1991) first classified instabilities for a falling Newtonian film on the exterior of a tube by applying the methods developed and explored by Bers (1983), Briggs (1964) and Huerre & Monkewitz (1990) among others. They identified a critical velocity separating absolute instability from convective instability for a two-dimensional KS equation, with the critical velocity dependent on the azimuthal mode number. Duprat *et al.* (2007) applied these techniques to a strongly nonlinear model similar to (2.21) with $We = 0$ for the exterior case. First finding a critical value for the thin-film parameter Bo^* and then transforming the thin-film dispersion relation to the long-wave dispersion relation through a substitution, Duprat *et al.* (2007) identified a condition on Bond number Bo^* and film thickness parameter a that must be met for films to be absolutely unstable. Camassa *et al.* (2014) later applied this approach to identify a threshold thickness for Newtonian films inside a tube; films thicker than this threshold were shown to be absolutely unstable, while thinner films were convectively unstable.

We briefly state this threshold condition for the Newtonian case. The dispersion relation of the Newtonian case (denoted by subscripts of N),

$$\omega_N = \frac{k_N}{2}(a^2 - 1 - 2\log a) + \frac{\mathrm{i}a^2}{16 Bo_N}(k_N^2 - k_N^4) f_1(1; a), \tag{3.8}$$

exhibits absolute instability if the criteria

$$\frac{2a^2 f_1(1; a)}{Bo_N(a^2 - 1 - 2\log a)} > 8(-17 + 7\sqrt{7})^{1/2} \tag{3.9}$$

is met, where Bo_N denotes the Bond number in the Newtonian case. This condition matches that found by Camassa *et al.* (2014) (adjusted for choice of scalings), and arises from considering branches of solutions to (3.8) found for complex wavenumber k and identifying parameter values at which distinct branches coalesce (see, e.g. Huerre & Monkewitz (1990), Duprat *et al.* (2007) and Camassa *et al.* (2014) for further discussion and a thorough derivation of this criteria).

How does the presence of elasticity affect this condition? The dispersion relation of the Newtonian case (3.8) may be transformed into (3.1) through the substitution

$$(k_N, \omega_N) = \left(1 + \frac{We\, Bo f_2(1; a)}{2a^3 f_1(1; a)}\right)^{-1/2} (k, \omega), \quad Bo_N = \left(1 + \frac{We\, Bo f_2(1; a)}{2a^3 f_1(1; a)}\right)^{-3/2} Bo. \tag{3.10a,b}$$

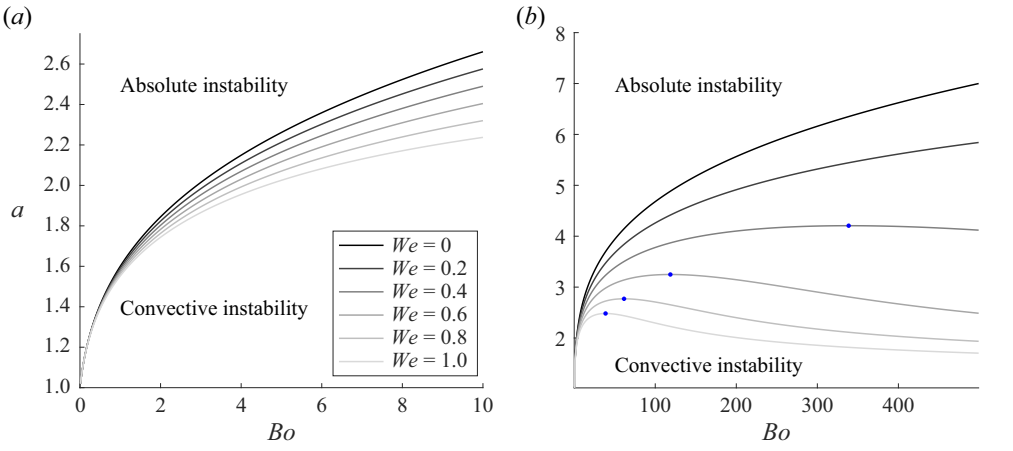

Figure 3. (*a*) Boundary in *Bo*-*a* space between absolute and convective instability for a variety of *We* values. (*b*) Same as panel (*a*) but for a larger range of *Bo* values. Blue dots denote maximum values of *a* obtained along each curve.

Substituting (3.10*a*,*b*) into (3.9) results in the following condition for absolute instability:

$$\frac{2Bo^{1/2}f_1(1;a)}{a(a^2-1-2\log a)}\left(\frac{a^2}{Bo}+\frac{Wef_2(1;a)}{2af_1(1;a)}\right)^{3/2} > 8(-17+7\sqrt{7})^{1/2}. \tag{3.11}$$

Figure 3 shows the *a*-*Bo* boundary between absolute and convective instability for a variety of *We* values. For $We = 0$, the boundary between absolute and convective instability monotonically increases with increasing *Bo*. For large values of *Bo* (or *a*), the boundary is governed by $Bo \approx a^4/[4(-17+7\sqrt{7})^{1/2}]$, which may be found by using $f_1(1;a) = a^4 + O(a^2)$ and $f_2(1;a) = 3a^4 + O(a^2)$ in (3.11).

Increasing *We* results in a greater region of absolute instability, with the effect most pronounced for larger *Bo* values. In contrast to the $We = 0$ case, the boundary for $We > 0$ exhibits non-monotonic behaviour, reaching some maximum attainable value of a_c for a given fixed positive *We*. This maximum value, denoted by blue dots in figure 3(*b*), occurs when $Bo = 4a^3f_1(1;a)/[Wef_2(1;a)]$. Past this value of *Bo*, the boundary decreases monotonically as $Bo \to \infty$, the scaling of which may be found in the thin-film limit by substituting $a = 1+\beta$ and $Bo = b\beta^\alpha$ into (3.11) with $\beta \ll 1$. This results in

$$\frac{16\beta^{1-\alpha}}{3b}(1+Web\beta^{\alpha+1})^{3/2} > 8(-17+7\sqrt{7})^{1/2}. \tag{3.12}$$

There are two consistent scalings possible, corresponding to one of the two terms inside parentheses providing the dominant balance with the right-hand side of (3.12). If the second term dominates, then $\alpha = -5$ and $Bo = 9(-17+7\sqrt{7})/4We^3\beta^5$, corresponding to the border between absolute and convective instability for large *Bo*. The other scaling, with $\alpha = 1$ and $Bo = 2\beta/[3(-17+7\sqrt{7})^{1/2}]$, corresponds to the border for small *Bo* and is independent of *We*.

4. Nonlinear results

In this section, the nonlinear equation (2.21) is solved numerically. Travelling wave solutions are found in § 4.2.

4.1. *Evolution equation*

A finite difference method was used to solve (2.21) numerically. Spatial derivatives were calculated using fourth-order approximations; time-stepping was done with an explicit second-order predictor-corrector method. An initial condition was prescribed by perturbing a constant free surface with a superposition of small-amplitude Fourier modes. In a typical simulation, 40 modes were used to perturb the free surface, though a variety of values were tried. The number of initial modes played a role in the transient dynamics as instabilities initially grew, but once the evolution had settled into a quasi-steady state, there was – in almost all cases – no clear signature of the initial conditions. The one exception to this is for films with a mean thickness very near the critical thickness – in which plug formation would only be triggered by wave mergers and not linear wave growth – where a change in initial conditions could result in a change of the final state (plug or no plug) in the finite-time simulations conducted. This was also noted in a study of Newtonian films with wall slip; see Schwitzerlett *et al.* (2023) for numerical tests and further discussion of this point.

At $z = 0$, inlet boundary conditions were prescribed by populating several ghost nodes upstream of the inlet using a periodic extension of the initial condition moving at the linear phase speed of the free-surface disturbances. At $z = L$, outlet boundary conditions were prescribed by populating several ghost nodes downstream of the inlet using a reflection of the final nodes within the domain. Other outlet boundary conditions were also tried; the exact prescription of these ghost nodes downstream only had a significant impact on the final few nodes near $z = L$, which will be largely ignored in the results. Simulations were also conducted using periodic boundary conditions. Since the dynamical outcomes of the simulations did not change when the boundary conditions were varied, these results are omitted, and results using inlet/outlet boundary conditions will be presented here.

Two dynamical outcomes are evident in simulation snapshots shown in figure 4(*a–c*). The baseline case in figure 4(*a*) shows a snapshot of the film in the tube using $Bo = 10$, $We = 0$ and $a = 1.8$. This snapshot is taken near $t = 500$, long after the dynamics have settled into a quasi-steady state. The gently perturbed film entering the domain at the inlet (left) is clearly convectively unstable, with disturbances growing as the film falls down the tube. Between $z = 100$ and $z = 150$, this growth saturates, with the remainder of the tube coated with a wavy film consisting of small-amplitude travelling-wave-like ripples.

A second outcome is shown in figure 4(*b*) with identical parameter values to figure 4)(*a*) except for $Bo = 5$. The film is still convectively unstable, but visible growth is seen closer to the inlet, e.g. near $z \approx 50$; the free-surface waves also have larger amplitude than with $Bo = 10$. However, the simulation is halted near $t = 150$ as one of the waves – near $z = 220$ – begins to undergo accelerated growth, with the free surface at the wave crest approaching $R = 0$ in finite time. Figure 4(*d*) shows the evolution of $\max R$ and $\min R$ over the domain as a function of time. As with other studies of asymptotic models, R approaching zero may be taken as the model's prediction that plug formation is about to occur. No attempt is made here to continue running the model forward past this time, as the nonlinearities in (2.21) include logarithms and inverse powers of R, preventing the model from being run forward as it is, though there has been interesting recent work in this direction. Most notably, Dietze *et al.* (2020) modified a WRIBL model for film flow inside a tube to prevent R from reaching a value of zero during plug formation; this was achieved through inclusion of a novel pressure term that allowed for arbitrarily narrow filaments of core fluid (air) to form where the model exhibited plug formation. Here, the focus is on whether plugs may be expected to form or not, and their propagation after formation is left for future work.

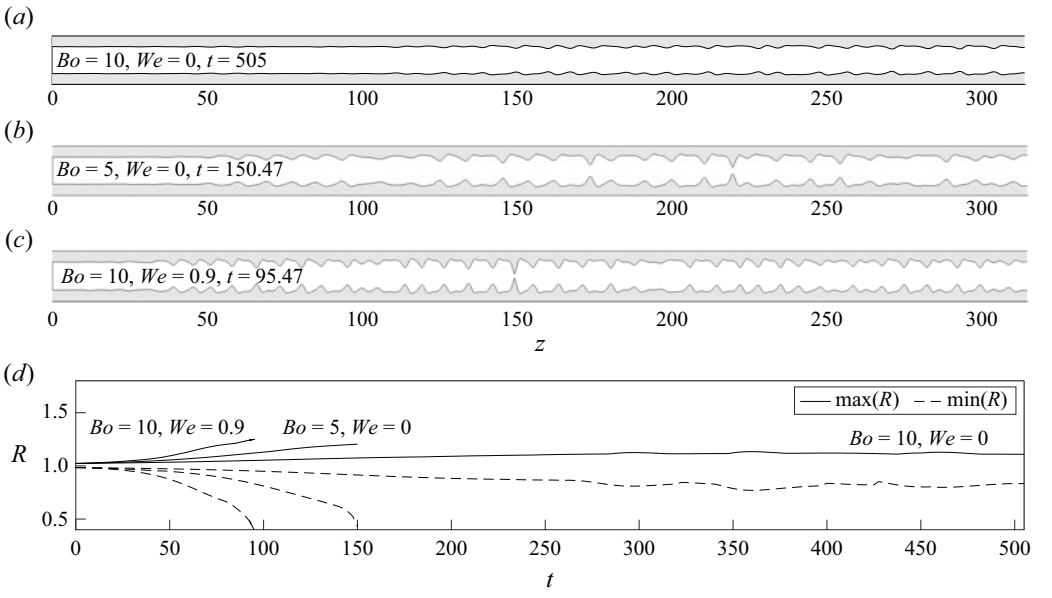

Figure 4. (*a–c*) Snapshots of the film evolution for $a = 1.8$ and for various Bo and We values. In panels (*b*,*c*), the snapshot is taken just prior to the formation of the first plug. (*d*) Maximum and minimum values of R over the domain in each simulation as a function of t.

Figure 4(*a*,*b*) indicates that for $a = 1.8$, there is some critical Bond number $5 < Bo_c < 10$ such that for $Bo > Bo_c$, plugs do not form; while for $Bo < Bo_c$, plugs do form. This is consistent with previous work (Camassa *et al.* 2014; Dietze *et al.* 2020; Ogrosky 2021) showing that stronger base flow inhibits plug formation in Newtonian films. The impact of viscoelasticity is examined next.

Figure 4(*c*) shows a snapshot of the film with $Bo = 10$, $We = 0.9$ and $a = 1.8$; note that all three panels of figure 4 have the same value of film thickness parameter a. Once again, the film is convectively unstable, though instability growth is visible even closer to the inlet, consistent with the higher linear growth rates found in § 3. The free-surface waves with $We > 0$ appear to have shorter typical wavelength than those with $We = 0$; e.g. in the simulation snapshots shown in figure 4, the average wavelength from $z = 100$ to $z = 300$ was approximately 9.5 in figure 4(*b*) and 7.7 in figure 4(*c*). This shorter average wavelength may be expected given the impact of viscoelasticity on wavelength shown in (3.5*a*,*b*). Similar to figure 4(*b*), the simulation was halted (near $t = 95$) as one wave – near $z = 150$ – underwent accelerated amplitude growth, resulting in $R \to 0$ indicating plug formation.

The results above indicate that either increasing We or decreasing Bo past some critical value while holding the film thickness constant results in plug formation. Said another way, for fixed Bo and We, there is a critical value of a such that if a exceeds this value, plug formation may be expected to occur; increasing We or decreasing Bo leads to a reduction in this critical value of a.

4.2. *Travelling wave solutions*

Since the free surface in figure 4 evolves into a travelling wave train, travelling wave solutions are sought next. Substituting $Q(Z) = Q(z - ct) = R(z, t)$ into (2.21) and

integrating once results in a third-order ordinary differential equation,

$$8cQ^2 + K + \left[1 - \frac{a^2}{Bo}\left(\frac{Q'}{Q^2} + Q'''\right)\right] f_1(Q;a) - \frac{We\,QQ'}{2a} f_2(Q;a) = 0, \qquad (4.1)$$

with speed c and constant of integration K. The approach used to find solutions to this ODE follows the approach outlined by Camassa *et al.* (2016) and is briefly outlined here. First, fixed point solutions are found for the three-dimensional dynamical system associated with (4.1); these correspond to constant solutions $Q = Q_0$. If the wave speed c is varied, a Hopf bifurcation in the solution family is identified using XPP/AUTO; XPP is a numerical tool for simulating and analysing dynamical systems (Ermentrout 2002) and also provides a front end to the numerical continuation and bifurcation package AUTO (Doedel *et al.* 2008). This bifurcation is a zero-Hopf bifurcation, which can be somewhat difficult to find numerically; to avoid this issue, a small viscosity-like term $\eta Q''$ was added to (4.1) which makes continuation onto a family of periodic solutions easier. Once periodic solutions have been found, the viscosity parameter η may be taken to zero. The mean value of Q^2 is ensured to be equal to one by imposing an integral condition. As the focus here is on waves with profiles similar to those seen in transient solutions like figure 4, only solution families with such profiles are presented here; other families, e.g. were considered by Zhou *et al.* (2016) for an integral boundary layer model.

Figure 5(a) shows several families of travelling wave solutions with period 4π for a variety of values of Bo and We; the period 4π was chosen as it is approximately the period of waves for $We = 0$ seen in figure 4(a) especially near the bottom of the tube, e.g. from $z = 150$ to $z = 250$. Each curve shows the wave amplitude of solutions within a family as a function of film thickness parameter. Before discussing the impact of viscoelasticity on these curves, we first note that each family has a turning point (denoted by a red dot) at some critical value a_c of the thickness parameter a. For $We = 0$, this critical thickness a_c has previously been shown to be a reliable proxy for the critical thickness required for plugs to form (Camassa *et al.* 2014, 2016; Ding *et al.* 2019; Dietze *et al.* 2020; Camassa *et al.* 2021). The critical thickness associated with the turning point solution depends on the value of Bo, with higher values of Bo corresponding to higher critical thickness, consistent with the results of § 4.1 and with the results of Dietze *et al.* (2020) showing that while the base flow does not contribute to the linear growth/decay of small disturbances, it plays a nonlinearly stabilizing role. Note that the horizontal axis shows $(a-1)/a$, with values close to 0 representing thin films, and values close to 1 representing thick films (since in the limit $a \to 1$ (thin films), $(a-1)/a \to 0$, while in the limit $a \to \infty$ (thick film), $(a-1)/a \to 1$). For each thickness $(a-1)/a$ less than the turning-point thickness, there are two travelling wave solutions found, one lying on a 'lower' branch with relatively small amplitude and one lying on an 'upper' branch with relatively large amplitude. Lower branch solutions are shown for several values of We in figure 5(c); these lower branch solutions correspond well to the waves seen in numerical simulations like those of figure 4(a–c). Upper branch solutions have a qualitatively similar shape, but are omitted here as waves with such large amplitude are not seen in numerical simulations (but see examples of these waves in, e.g. Camassa *et al.* 2014 for a Newtonian film).

How does the presence of viscoelasticity impact the critical thickness associated with the turning point of solution families? Figure 5(a) shows that as We increases, this turning-point thickness – which serves as a proxy for the critical thickness required for plugs to form – decreases, again consistent with the results of § 4.1 showing that viscoelasticity promotes plug formation. The impact is most pronounced for larger values of Bo. Figure 5(b) shows the solution corresponding to the turning point denoted in red in panel (a) for $Bo = 10$; as We increases, the support of these waves decreases significantly.

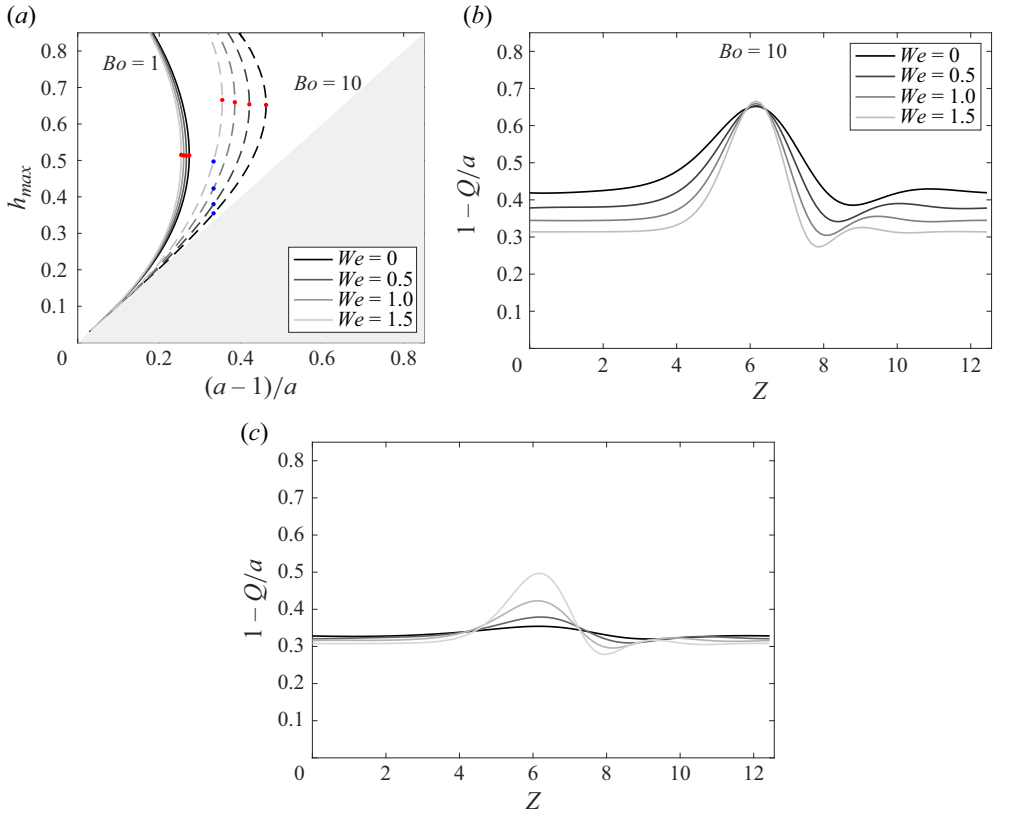

Figure 5. (*a*) Families of travelling wave solutions with $Bo = 1$ and $Bo = 10$ for four values of We. Turning points indicated by red dots. (*b*) Travelling wave solutions with $Bo = 10$ corresponding to red dots in panel (*a*). (*c*) Travelling wave solutions with $Bo = 10$ and $a = 1.5$ corresponding to blue dots in panel (*a*).

While some of this change in support could be attributed to the different film thickness of each wave, viscoelasticity also plays a role; to demonstrate this, figure 5(*c*) shows travelling wave solutions (corresponding to blue dots in figure 5*c*) for fixed a and Bo and various We. Despite having uniform thickness, the change in support persists, most noticeable when one observes the markedly different distance from wave crest to the trough (capillary ripple) that precedes the crest.

How does the turning point in travelling wave solution families depend on the chosen period size? Figure 6(*a*) shows the dependence of a_c on period for $We = 0$ and $We = 1.5$. For both curves, there appears to be a value of a_c which the curves approach asymptotically in the limit of large period, while for small period, the value of a_c increases rather sharply. The period 4π is denoted along both curves by a (blue or red) dot.

Given that figure 4(*a–c*) indicates that elasticity produces waves with shorter wavelength, it may be that a more accurate estimate of the critical thickness would be provided by a turning point found for shorter-wavelength travelling wave solutions for $We > 0$. Figure 6(*b*) shows the $Bo = 10$ travelling wave solution families for $We = 0$ and $We = 1.5$ for period 4π (dashed lines), as well as the solution family for $We = 1.5$ and period ≈ 8.5 (solid line). This shorter wavelength produces a turning point at a larger value of a_c than the 4π domain waves, as expected.

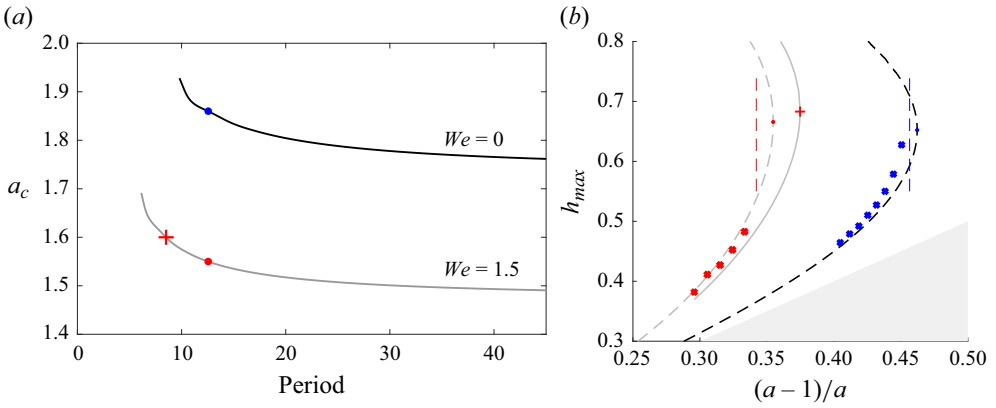

Figure 6. (*a*) Dependence of a_c on period size for $We = 0$ and $We = 1.5$. (*b*) Families of travelling wave solutions with $Bo = 10$ for $We = 0$ and $We = 1.5$; dashed grey and black lines show period 4π solutions (corresponding to the dots in panel *a*), solid grey line shows period ≈ 8.5 solutions (corresponding to red $\times$ in panel *a*). Thick dots denote the maximum value of h_{max} during numerical simulations of (2.21); see text for details. Vertical (red and blue) dashed lines indicate thickness at which plugs formed in nonlinear simulations.

To assess which period length better predicts the critical thickness in model solutions, an additional test was conducted. Model solutions were found using an initial condition with a thickness well below the critical thickness. Once the free surface had settled into a quasi-steady state, the film thickness was increased by a small amount. This process was repeated until the simulation indicated plug formation through $R \to 0$ in finite time. The average value of $\min_z R$ was calculated over a period once a quasi-steady state had been achieved for each thickness; the resulting data points are plotted in figure 6(*b*) for $We = 0$ and $We = 1.5$, with the thickness resulting in plug formation indicated by a vertical dashed line. It appears that for both the Newtonian and non-Newtonian films, the 4π solutions provide a reasonable estimate of the critical thickness.

How does a_c depend on Bo for various values of We? Figure 7 shows the dependence of the critical thickness parameter a_c on Bo and We; panel (*a*) shows this dependence with various fixed Bo while in panel (*b*), We is held fixed. For $We = 0$, the critical thickness increases arbitrarily with increasing Bo. Ogrosky (2021) noted that for Newtonian flow ($We = 0$), there appeared to be a scaling law between Bo and a_c in the limit of strong base flow (weak surface tension), i.e. $Bo \to \infty$; an empirical fit was found with a 1/5 scaling. Here, we note that the scaling appears to lie somewhere between 1/5 and 1/6 in figure 7(*b*). A brief justification (relying partially on numerical observations) for the existence of a scaling law is given in Appendix A, where the relationship

$$Bo \propto \frac{a_c^6}{\log a_c} \tag{4.2}$$

is identified for $a_c \to \infty$. Thus, in the absence of elasticity, a film may be arbitrarily thick and still not form plugs, provided the base flow is strong enough relative to the effects of surface tension.

For small values of Bo, the presence of elasticity only slightly modifies the value of a_c, consistent with the results of figure 5(*a*). The curves for various fixed We nearly overlap for small Bo and approach a value corresponding to a film thickness of 12 % of the tube radius (denoted with a grey horizontal dashed line). This percentage has been identified

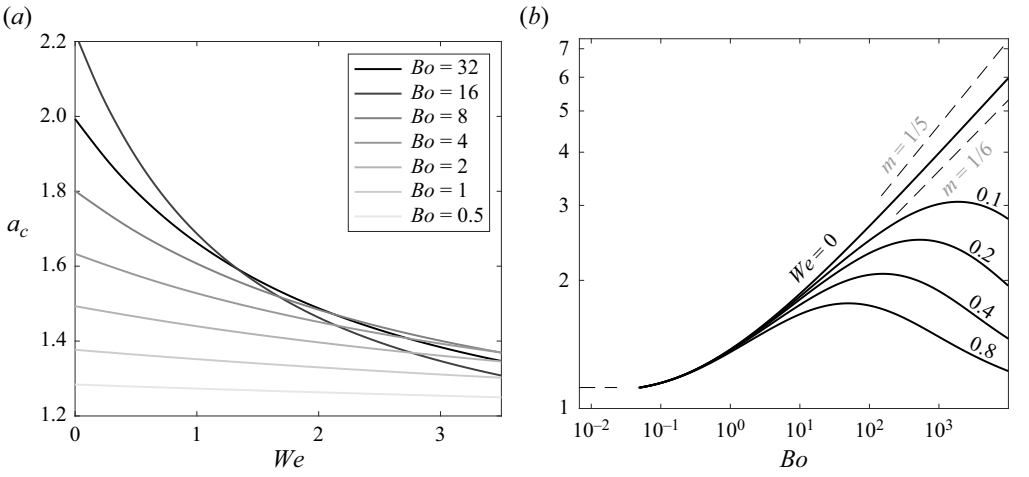

Figure 7. (*a*) Critical thickness a_c as a function of *We* for various fixed values of *Bo*. (*b*) a_c versus *Bo* for various fixed values of *We*. Grey dashed lines show slopes $m = 1/5$ and $m = 1/6$; black dashed line shows the approximate critical thickness for vanishing *Bo*.

in previous studies with thin-film models as an approximate estimate of the thickness required for plugs to form (Gauglitz & Radke 1988) in a surface-tension dominated limit.

In contrast to the Newtonian case, however, there is now a maximum value of a_c that is attainable for some *Bo* at a given fixed $We > 0$; past this *Bo* value, the critical thickness a_c decreases monotonically. Some intuition for this result may be found by revisiting the temporal linear stability analysis. Recall that the maximum growth rate is given by

$$GR_{max} = \frac{a^2 f_1(1;a)}{16Bo}(k_{max}^2 - k_{max}^4) + \frac{Wef_2(1;a)}{32a}k_{max}^2, \tag{4.3}$$

where k_{max} is given in (3.5*a*,*b*). Substituting (3.5*a*,*b*) into (4.3), taking a derivative with respect to *Bo* and setting equal to zero, a local minimum in GR_{max} as a function of *Bo* may be found at $Bo = 2a^3 f_1(1;a)/Wef_2(1;a)$ (or alternately, when $k_{max} = 1$). This is depicted in figure 8, in which growth rate curves for $We = 0.8$ and $a = 1.4$ are shown for various *Bo* values. The dependence of GR_{max} on *Bo* (through k_{max} in (3.5*a*,*b*)) is shown by the dashed line. For these fixed values of *a* and *We*, there is some value of *Bo* for which the growth rate is minimized over all *Bo*. While a minimum in the (linear) growth rate cannot be expected to exactly correspond to a maximum in critical thickness, it seems reasonable to conjecture that the existence of such a minimum may indicate a value of *Bo* for which linear instabilities may more readily saturate in the nonlinear regime, suppressing plug formation and allowing for a relatively large value of a_c.

It is important to note that the addition of polymers to a previously Newtonian film not only introduces elasticity (modifying *We*) but can also change the surface tension of the film (modifying *Bo*). Thus, if polymers reduce the film's surface tension, it is possible that their presence could actually inhibit plug formation, despite the plug-promoting role of elasticity. It may be important, therefore, to quantify the dependence of a_c on both *Bo* and *We*, particularly for $We \ll 1$. Similar to figure 7, figure 9(*a*) shows curves containing turning point solutions but now for various fixed values of a_c. Each of these curves reaches a maximum value of *We*, consistent with the discussion regarding figure 7. The blue dashed lines are tangent lines to each curve at $We = 0$, and indicate the slope or $(\partial Bo/\partial We)|_{We=0}$ for isolines of a_c. Those slopes are also shown in figure 9(*b*) by the three blue dots, with

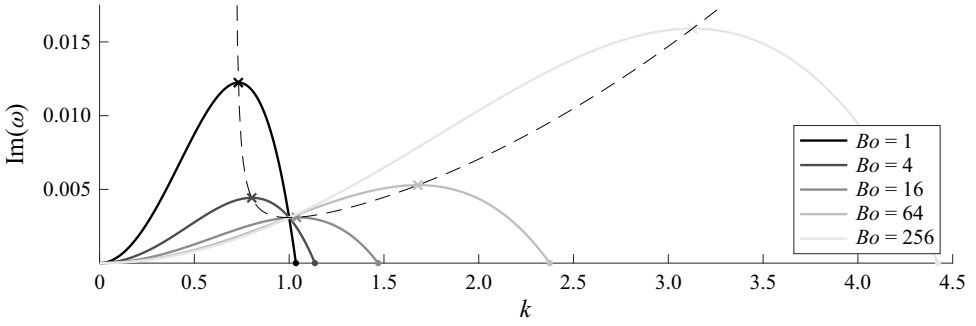

Figure 8. Growth rates of (2.21) for $a = 1.4$, $We = 0.8$ and various values of Bo. $\times$ symbols denote the maximum growth rate GR_{max}, and $\cdot$ symbols denote cutoff wavenumber k_c. Black dashed line indicates dependence of GR_{max} on Bo through k_{max} defined in (3.5*a*,*b*).

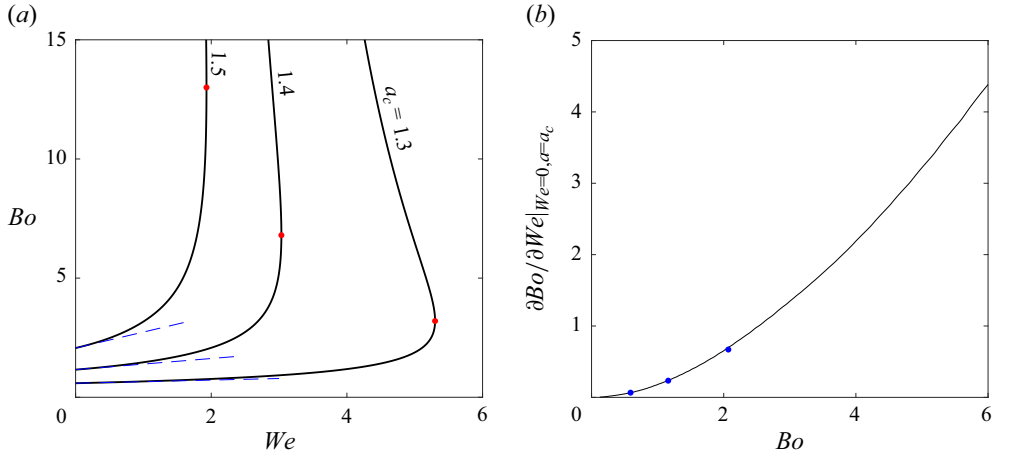

Figure 9. (*a*) Critical thickness a_c isolines as a function of We and Bo. Also shown are the maximum value of We for fixed a_c (red dots) and the tangent line to each curve at $We = 0$ (blue dashed lines). (*b*) Derivative $\partial Bo_c/\partial We_c|_{We=0,a=a_c}$ plotted as a function of Bo (see text for interpretation of this term).

the black curve showing the dependence of this slope on Bo. This dependence indicates that the slope $(\partial Bo/\partial We)|_{We=0}$ scales with Bo^2.

For example, if polymers are introduced to a Newtonian film with $a_c = 1.5$, the impact on plug formation is as follows: if the polymers increase Bo by an amount greater than $We \times (\partial Bo/\partial We)|_{We=0} \approx 1.0We$, plug formation will be suppressed. If, however, Bo increases by less than this, or is unchanged or decreases, then plug formation will be promoted by the addition of polymers.

Before concluding, we summarize the model results on plug formation and instability classification (absolute versus convective) in figure 10. The combinations of Bo and a values that produce each outcome are shown in figure 10(*a*) for several values of We and small to moderate Bo; figure 10(*b*) shows this for higher values of Bo, highlighting the dramatic effect an increase in We has for large values of Bo. Note also that, for some small Bo (e.g. $Bo \approx 0.125$ for $We = 0$), the AI/CI boundary and the plug/no-plug boundary cross, indicating the possibility of absolutely unstable films that do not form plugs for $Bo \lesssim 0.125$.

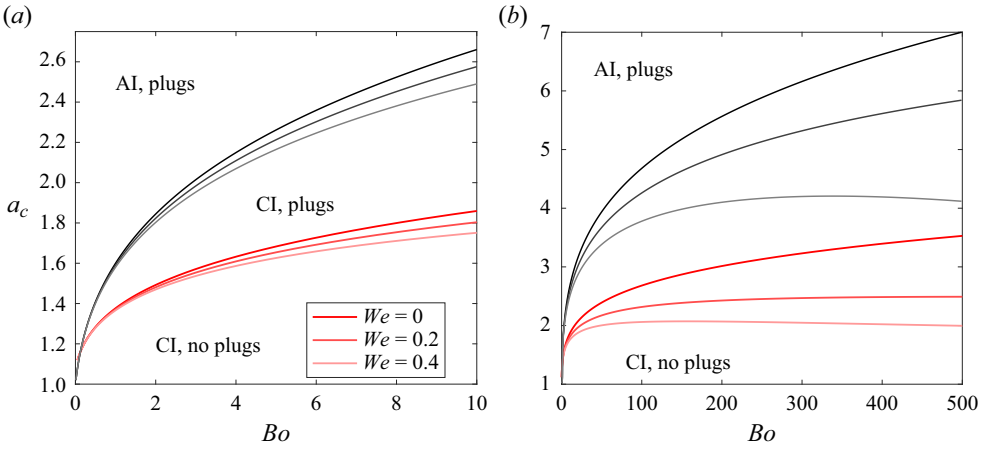

Figure 10. (*a*) Boundary separating plug formation from no plug formation as determined by turning points in travelling wave families (red lines), and the boundary separating absolutely unstable films from convectively unstable films (grey lines), shown for three values of *We*. (*b*) Same as panel (*a*) but for larger values of *Bo*.

5. Conclusion

We have developed a long-wave asymptotic model for a viscoelastic falling film inside a tube. An upper convected Maxwell model was used to incorporate viscoelasticity; the resulting model equation is identical to that obtained using an Oldroyd-B model (up to first-order). Linear stability analysis allowed the impact of elasticity on the cutoff wavenumber and wavenumber of maximum growth rate to be determined analytically. Similarly, the impact of elasticity on the classification of instabilities as absolute or convective was determined, with elasticity promoting absolute instability. The impact of elasticity was more pronounced as the Bond number increased. In contrast to the Newtonian case, for $We > 0$, the AI/CI boundary exhibits non-monotonic behaviour with increasing *Bo*.

Numerical solutions to the model equation show that elasticity promotes plug formation. Travelling wave solution families were found, and the turning points in those families may be used as a proxy for the critical thickness required for plugs to form. By continuation of these turning points, the impact of elasticity on plug formation is easily demonstrated throughout parameter space. In contrast to the Newtonian version of the model (in which plug formation can be suppressed in a film of any thickness, provided the base flow is strong enough), any amount of elasticity creates a maximum critical thickness, past which plugs form regardless of the base flow strength.

The addition of polymers to a Newtonian film may not only introduce elasticity but also modify the surface tension. The trade-off between increasing *We* (which promotes instability growth and plug formation) and increasing *Bo* (which inhibits instability growth and plug formation) was explored.

It would be interesting to test the impact of other constitutive equations on these results, particularly on the large impact that increasing *We* has on a_c for large values of *Bo*; this is left for future work.

One potential application of this information relates to the airway surface liquid lining human airways. It is well established that this highly viscous fluid is viscoelastic, and the information provided here may be important in accounting for plug formation and rupture

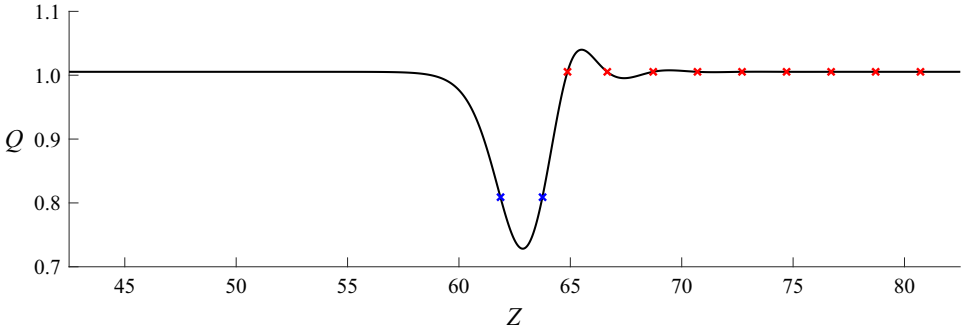

Figure 11. Limit point travelling wave solution with $Bo = 1$, $We = 0$, period 40π; solution domain is $[0, 40\pi]$ but solution is only shown near wave crest for clarity. Red (blue) $\times$ symbols denote locations where $Q = Q_s$ ($Q = Q^*$).

in human airway models, specifically in upper airways where gravity may be expected to play a role in the lining's evolution.

Funding. This work was supported by the Simons Foundation, no. 854116, by the National Science Foundation under grants RTG DMS-0943851, DMS-1009750, DMS-1517879, DMS-1910824, DMS-2308063, and by the Office of Naval Research under grants N00014-18-1-2490, N00014-23-1-2478, DURIP N00014-12-1-0749.

Declaration of interests. The authors report no conflict of interest.

Author ORCID.
H. Reed Ogrosky https://orcid.org/0000-0002-5848-834X.

Appendix A. Scaling law for turning point solutions with $We = 0$ and large Bo

In figure 7(*b*), there appears to be a scaling law between Bo and a_c for Newtonian films as $Bo \to \infty$ (or, alternatively, $a_c \to \infty$). A brief justification for this will be given here. For simplicity, a wave with very large period will be considered here, though the idea may be readily adapted to the solutions shown in the text. Recall that an integral condition is enforced when finding travelling wave solutions with period L: $(1/L)\int_0^L Q^2\,\mathrm{d}Z = 1$.

In all of the travelling wave solutions computed here, there are two values of Q for which $Q'/Q^2 + Q''' = 0$. One of these corresponds to the substrate thickness Q_s far away from the wave crest; for very large-domain waves, this value $Q_s \approx 1$. This value is obtained at many values of Z downstream of the wave. Figure 11 shows a limit point travelling wave solution with $Bo = 1$, $We = 0$ and extended period of 40π; red $\times$ symbols denote locations where $Q(Z)$ obtains this value Q_s.

At any such location along the profile where Q attains this value, (4.1) simplifies to

$$K = -8c - f_1(1; a). \tag{A1}$$

Substituting (A1) into (4.1) results in

$$8c(Q^2 - 1) - f_1(1; a) + f_1(Q; a) = \frac{a^2}{Bo}\left(\frac{Q'}{Q^2} + Q'''\right) f_1(Q; a). \tag{A2}$$

The second value of Q for which $Q'/Q^2 + Q''' = 0$, denoted here as $Q^* < Q_s$, is obtained exactly twice in the single-hump travelling wave solutions computed here – once

on the leading edge and once on the trailing edge of the wave crest. These points are denoted by blue $\times$ symbols in figure 11. At these points, (A2) becomes

$$8c[(Q^*)^2 - 1] - f_1(1; a) + f_1(Q^*; a) = 0, \tag{A3}$$

which can be solved for c to get

$$c = \frac{a^2}{2} - \frac{(Q^*)^2 - 1}{2[(Q^*)^2 - 1]} \log a - 3[(Q^*)^4 - 1] + 4(Q^*)^4 \log Q^*. \tag{A4}$$

Next, this expression for c may be plugged into the full travelling wave equation to get (after simplification)

$$\left[-\frac{4[(Q^*)^4 - 1](Q^2 - 1)}{(Q^*)^2 - 1} + 4(Q^4 - 1) \right] \log a + O(1) = \frac{a^2}{Bo} \left(\frac{Q'}{Q^2} + Q''' \right) \left(a^4 - 4a^2Q^2 + 3Q^4 + 4Q^4 \log \frac{a}{Q} \right). \tag{A5}$$

One additional numerical observation is that as a gets larger, it appears to be the case for solutions computed here that $Q'/Q^2 + Q''' = O(1)$ for turning point solutions. Using this observation in (A5), it is clear that for large a, we must have

$$Bo \propto \frac{a^6}{\log a}. \tag{A6}$$

Appendix B. Long-wave Oldroyd-B model

If the upper convected Maxwell constitutive model is replaced by the Oldroyd-B model, where the deviatoric stress can be split into the sum of a Newtonian (viscous) component and an extra stress τ, the constitutive model (2.2) is replaced by

$$\bar{\sigma}_{\bar{r}\bar{r}} = 2\bar{\mu}_s \partial_{\bar{r}} \bar{u} + \bar{\tau}_{\bar{r}\bar{r}}, \tag{B1a}$$

$$\bar{\sigma}_{\bar{r}\bar{z}} = \bar{\mu}_s (\partial_{\bar{z}} \bar{u} + \partial_{\bar{r}} \bar{w}) + \bar{\tau}_{\bar{r}\bar{z}}, \tag{B1b}$$

$$\bar{\sigma}_{\bar{z}\bar{z}} = 2\bar{\mu}_s \partial_{\bar{z}} \bar{w} + \bar{\tau}_{\bar{z}\bar{z}}, \tag{B1c}$$

where $\bar{\mu}_s$ is the viscosity of the Newtonian solvent and where the extra stress is modelled by

$$\bar{\tau}_{\bar{r}\bar{r}} + \bar{\lambda}_1 [\partial_{\bar{t}} \bar{\tau}_{11} + \bar{u} \partial_{\bar{r}} \bar{\tau}_{\bar{r}\bar{r}} + \bar{w} \partial_{\bar{z}} \bar{\tau}_{\bar{r}\bar{r}} - 2(\partial_{\bar{r}} \bar{u} \bar{\tau}_{\bar{r}\bar{r}} + \partial_{\bar{z}} \bar{u} \bar{\tau}_{\bar{r}\bar{z}})] = 2\bar{\mu}_p \partial_{\bar{r}} \bar{u}, \tag{B2a}$$

$$\bar{\tau}_{\bar{r}\bar{z}} + \bar{\lambda}_1 [\partial_{\bar{t}} \bar{\tau}_{12} + \bar{u} \partial_{\bar{r}} \bar{\tau}_{\bar{r}\bar{z}} + \bar{w} \partial_{\bar{z}} \bar{\tau}_{\bar{r}\bar{z}} - (\partial_{\bar{r}} \bar{w} \bar{\tau}_{\bar{r}\bar{r}} + (\partial_{\bar{r}} \bar{u} + \partial_{\bar{z}} \bar{w}) \bar{\tau}_{\bar{r}\bar{z}}) + \partial_{\bar{z}} \bar{u} \bar{\tau}_{\bar{z}\bar{z}}] = \bar{\mu}_p (\partial_{\bar{z}} \bar{u} + \partial_{\bar{r}} \bar{w}), \tag{B2b}$$

$$\bar{\tau}_{\bar{z}\bar{z}} + \bar{\lambda}_1 [\partial_{\bar{t}} \bar{\tau}_{22} + \bar{u} \partial_{\bar{r}} \bar{\tau}_{\bar{z}\bar{z}} + \bar{w} \partial_{\bar{z}} \bar{\tau}_{\bar{z}\bar{z}} - 2(\partial_{\bar{r}} \bar{w} \tau_{\bar{r}\bar{z}} + \partial_{\bar{z}} \bar{w} \bar{\tau}_{\bar{z}\bar{z}})] = 2\bar{\mu}_p \partial_{\bar{z}} \bar{w}, \tag{B2c}$$

where $\bar{\lambda}_1$ is the relaxation time, $\bar{\mu}_p$ is the polymeric viscosity and $\bar{\mu}_0 = \bar{\mu}_s + \bar{\mu}_p$ is the total viscosity (Bird, Armstrong & Hassager 1987; Zhang, Matar & Craster 2002).

We next non-dimensionalize (2.1), (B1)–(B2), (2.3)–(2.4) using scales (2.5*a–g*) with $\bar{W}_0 = \bar{\rho}\bar{g}\bar{R}_0^2/\bar{\mu}_0$ and $\tau_{ij} = \bar{\tau}_{ij}/(\bar{\rho}\bar{g}\bar{R}_0)$.

Substituting these scales in (B1) and (B2) results in

$$\sigma_{rr} = 2\epsilon(1-\mu)u_r + \tau_{rr}, \tag{B3a}$$

$$\sigma_{rz} = (1-\mu)(\epsilon^2 u_z + w_r) + \tau_{rz}, \tag{B3b}$$

$$\sigma_{zz} = 2\epsilon(1-\mu)w_z + \tau_{zz}, \tag{B3c}$$

and

$$\tau_{rr} + \epsilon\widetilde{We}[\partial_t\tau_{rr} + u\partial_r\tau_{rr} + w\partial_z\tau_{rr} - 2(\partial_r u)\tau_{rr} - 2\epsilon(\partial_z u)\tau_{rz}] = 2\epsilon\mu\partial_r u, \tag{B4a}$$

$$\begin{aligned}\tau_{rz} + \widetilde{We}[\epsilon\partial_t\tau_{rz} + \epsilon u\partial_r\tau_{rz} + \epsilon w\partial_z\tau_{rz} - (\partial_r w)\tau_{rr} - \epsilon(\partial_r u + \partial_z w)\tau_{rz} - \epsilon^2(\partial_z u)\tau_{zz}] \\ = \mu(\epsilon^2\partial_z u + \partial_r w),\end{aligned} \tag{B4b}$$

$$\tau_{zz} + \widetilde{We}[\epsilon\partial_t\tau_{zz} + \epsilon u\partial_r\tau_{zz} + \epsilon w\partial_z\tau_{zz} - 2(\partial_r w)\tau_{rz} - 2\epsilon(\partial_z w)\tau_{zz}] = 2\epsilon\mu\partial_z w, \tag{B4c}$$

respectively, where $\widetilde{We} = \bar{\lambda}_1\bar{W}_0/\bar{R}_0$ is the Weissenberg number and $\mu = \bar{\mu}_p/\bar{\mu}_0$. Continuing the long-wave model derivation as before produces the final model equation

$$\partial_t R = \frac{1}{16R}\partial_z\left[f_1(R;a)\left(1 - \frac{a^2}{Bo}\left(\frac{\partial_z R}{R^2} + \partial_{zzz}R\right)\right) - \frac{\mu We R(\partial_z R)}{2a}f_2(R;a)\right]. \tag{B5}$$

References

Bahrani, S.A., Hamidouche, S., Moazzen, M., Seck, K., Duc, C., Muradoglu, M., Grotberg, J.B. & Romano, F. 2022 Propagation and rupture of elastoviscoplastic liquid plugs in airway reopening model. *J. Non-Newtonian Fluid Mech.* **300**, 104718.

Benney, D. 1966 Long waves in liquid films. *J. Math. Phys.* **45**, 150–155.

Bers, A. 1983 Space-time evolution of plasma instabilities-absolute and convective. In *Handbook of Plasma Physics* (ed. M.N. Rosenbluth & R.Z. Sagdeev), vol. I, pp. 451–517. North-Holland.

Bird, R.B., Armstrong, R.C. & Hassager, O. 1987 *Dynamics of Polymeric Liquids*, vol. 1, 2nd edn. John Wiley.

Bottier, M., Peña Fernández, M., Pelle, G., Isabey, D., Louis, B., Grotberg, J.B. & Filoche, M. 2017 A new index for characterizing micro-bead motion in a flow induced by ciliary beating. Part 2. Modeling. *PLoS Comput. Biol.* **13** (7), e1005552.

Bottier, M., *et al.* 2017 A new index for characterizing micro-bead motion in a flow induced by ciliary beating. Part 1. Experimental analysis. *PLoS Comput. Biol.* **13** (7), e1005605.

Boulogne, F., Fardin, M.A., Lerouge, S., Pauchard, L. & Giorgiutti-Dauphiné, F. 2013 Suppression of the Rayleigh-Plateau instability on a vertical fibre coated with wormlike micelle solutions. *Soft Matt.* **9**, 7787–7796.

Boulogne, F., Pauchard, L. & Giorgiutti-Dauphiné, F. 2012 Instability and morphology of polymer solutions coating a fibre. *J. Fluid Mech.* **704**, 232–250.

Briggs, R.J. 1964 *Electron-Stream Interaction with Plasmas*. MIT Press.

Camassa, R. & Lee, L. 2006 *Advances in Engineering Mechanics – Reflections and Outlooks* (ed. A. Chwang, M. Teng & D. Valentine), 222–238. World Scientific.

Camassa, R., Marzuola, J., Ogrosky, H.R. & Swygert, S. 2021 On the stability of traveling wave solutions to thin-film and long-wave models for film flows inside a tube. *Physcia* D **415**, 132750.

Camassa, R., Marzuola, J., Ogrosky, H.R. & Vaughn, N. 2016 Traveling waves for a model of gravity-driven film flows in cylindrical domains. *Physica* D **333**, 254–265.

Camassa, R., Ogrosky, H.R. & Olander, J. 2014 Viscous film flow coating the interior of a vertical tube. Part 1. Gravity-driven flow. *J. Fluid Mech.* **745**, 682–715.

Chen, Z., Zhong, M., Luo, Y., Deng, L., Hu, Z. & Song, Y. 2019 Determination of rheology and surface tension of airway surface liquid: a review of clinical relevance and measurement techniques. *Respir. Res.* **20**, 274.

Choudhury, A., Filoche, M., Ribe, N.M., Grenier, N. & Dietze, G.F. 2023 On the role of viscoelasticity in mucociliary clearance: a hydrodynamic continuum approach. *J. Fluid Mech.* **971**, A33.

Craster, R.V. & Matar, O.K. 2006 On viscous beads flowing down a vertical fibre. *J. Fluid Mech.* **553**, 85–105.

CRASTER, R.V. & MATAR, O.K. 2009 Dynamics and stability of thin liquid films. *Rev. Mod. Phys.* **81** (3), 1131–1198.

DEISSLER, R.J., ORON, A. & LEE, Y.C. 1991 Evolution of two-dimensional waves in externally perturbed flow on a vertical cylinder. *Phys. Rev.* A **43** (8), 4558–4561.

DIETZE, G., LAVALLE, G. & RUYER-QUIL, C. 2020 Falling liquid films in narrow tubes: occlusion scenarios. *J. Fluid Mech.* **894**, A17.

DIETZE, G.F. & RUYER-QUIL, C. 2015 Films in narrow tubes. *J. Fluid Mech.* **762**, 68–109.

DING, Z., LIU, Z., LIU, R. & YANG, C. 2019 Thermocapillary effect on the dynamics of liquid films coating the interior surface of a tube. *Intl J. Heat Mass Transfer* **138**, 524–533.

DOEDEL, E.J., CHAMPNEYS, A.R., DERCOLE, F., FAIRGRIEVE, T., KUZNETSOV, Y., OLDEMAN, B., PAFFENROTH, R., SANDSTEDE, B.J., WANG, X. & ZHANG, C. 2008 *AUT0-07P: Continuation and Bifurcation Software for Ordinary Differential Equations*. Montreal Concordia University.

DUPRAT, C., RUYER-QUIL, C., KALLIADASIS, S. & GIORGIUTTI-DAUPHINE, F. 2007 Absolute and convective instabilities of a viscous film flowing down a vertical fiber. *Phys. Rev. Lett.* **98**, 244502.

ERKEN, O., FAZLA, B., ROMANO, F., GROTBERG, J.B., IZBASSAROV, D. & MURADOGLU, M. 2023 Effects of elastoviscoplastic properties of mucus on airway closure in healthy and pathological conditions. *Phys. Rev. Fluids* **8**, 053102-1–26.

ERMENTROUT, B. 2002 *Simulating, Analyzing, and Animating Dynamical Systems: A Guide to XPPAUT for Researchers and Students*. Society for Industrial and Applied Mathematics.

FRENKEL, A.L. 1992 Nonlinear theory of strongly undulating thin films flowing down vertical cylinders. *Europhys. Lett.* **18**, 583–588.

FUJIOKA, H., HALPERN, D., RYANS, J. & GAVER III, D.J. 2016 Reduced-dimension model of liquid plug propagation in tubes. *Phys. Rev. Fluids* **1**, 053201.

GAUGLITZ, P. & RADKE, C. 1988 An extended evolution equation for liquid film breakup in cylindrical capillaries. *Chem. Engng Sci.* **43** (7), 1457–1465.

GOREN, S.L. 1962 The instability of an annular thread of fluid. *J. Fluid Mech.* **12** (2), 309–319.

GROTBERG, J.B. & JENSEN, O.E. 2004 Biofluid mechanics in flexible tubes. *Annu. Rev. Fluid Mech.* **36**, 121–147.

HALPERN, D., FUJIOKA, H. & GROTBERG, J.B. 2010 The effect of viscoelasticity on the stability of a pulmonary airway liquid layer. *Phys. Fluids* **22**, 011901.

HAMMOND, P.S. 1983 Nonlinear adjustment of a thin annular film of viscous fluid surrounding a thread of another within a circular pipe. *J. Fluid Mech.* **137**, 363–384.

HICKOX, C.E. 1971 Instability due to viscosity and density stratification in axisymmetric pipe flow. *Phys. Fluids* **14** (2), 251–262.

HUERRE, P. & MONKEWITZ, P.A. 1990 Local and global instabilities in spatially developing flows. *Annu. Rev. Fluid Mech.* **22**, 473–537.

JENSEN, O.E. 2000 Draining collars and lenses in liquid-lined vertical tubes. *J. Colloid Interface Sci.* **221**, 38–49.

JI, H., FALCON, C., SADEGHPOUR, A., ZENG, Z., JU, Y.S. & BERTOZZI, A.L. 2019 Dynamics of thin liquid films on vertical cylindrical fibres. *J. Fluid Mech.* **865**, 303–327.

KALLIADASIS, S. & CHANG, H.-C. 1994 Drop formation during coating of vertical fibres. *J. Fluid Mech.* **261**, 135–168.

KANG, F. & CHEN, K.P. 1995 Nonlinear elastic instability of gravity-driven flow of a thin viscoelastic film down an inclined plane. *J. Non-Newtonian Fluid Mech.* **57**, 243–252.

KAPITZA, P.L. 1948 Wave flow of thin layer of viscous fluid. *Zh. Eksp. Teor. Fiz.* **18**, 3–28.

KERCHMAN, V. & FRENKEL, A. 1994 Interactions of coherent structures in a film flow: simulations of a highly nonlinear evolution equation. *Theor. Comput. Fluid Dyn.* **6** (4), 235–254.

KHAYAT, R.E. & KIM, K.-T. 2006 Thin-film flow of a viscoelastic fluid on an axisymmetric substrate of arbitrary shape. *J. Fluid Mech.* **552**, 37–71.

KIM, C.S., GREENE, M.A., SANKARAN, S. & SACKNER, M.A. 1986 Mucus transport in the airways by two-phase gas-liquid flow mechanism: continuous flow model. *J. Appl. Physiol.* **60**, 908–917.

KIM, C.S., IGLESIAS, A.J. & SACKNER, M.A. 1987 Mucus clearance by two-phase gas-liquid flow mechanism: asymmetric periodic flow model. *J. Appl. Physiol.* **62**, 959–971.

KIM, C.S., RODRIGUEZ, C.R., ELDRIDGE, M.A. & SACKNER, M.A. 1986 Criteria for mucus transport in the airways by two-phase gas-liquid flow mechanism. *J. Appl. Physiol.* **60**, 901–907.

KLIAKHANDLER, I., DAVIS, S.H. & BANKOFF, S. 2001 Viscous beads on vertical fibre. *J. Fluid Mech.* **429**, 381–390.

LAI, S.K., WANG, Y.-Y., WIRTZ, D. & HANES, J. 2009 Micro- and macrorheology of mucus. *Adv. Drug Deliv. Rev.* **61**, 86–100.

OGROSKY, H.R. 2021 Linear stability and nonlinear dynamics in a long-wave model of film flows inside a tube in the presence of surfactant. *J. Fluid Mech.* **908**, A23.

OLANDER, J. 2020 Newtonian and non-Newtonian flows in a simple model of the human trachea. Dissertation, University of North Carolina.

ORON, A., DAVIS, S.H. & BANKOFF, S.G. 1997 Long-scale evolution of thin liquid films. *Rev. Mod. Phys.* **69** (3), 931.

PATNE, R. 2021 Purely elastic instabilities in the airways and oral area. *J. Fluid Mech.* **928**, A22.

PATNE, R. 2024 Effect of inhaled air temperature on mucus dynamics in the proximal airways. *J. Fluid Mech.* **978**, A15.

ROMANO, F., MURADOGLU, M., FUJIOKA, H. & GROTBERG, J.B. 2021 The effect of viscoelasticity in an airway closure model. *J. Fluid Mech.* **913**, A31.

RUYER-QUIL, C. & MANNEVILLE, P. 1998 Modeling film flows down inclined planes. *Eur. J. Phys.* B **6**, 277–292.

SCHWITZERLETT, M., OGROSKY, H.R. & TOPALOGLU, I. 2023 A long-wave model for film flow inside a tube with slip. *J. Fluid Mech.* **974**, A22.

SHAQFEH, E.S.G., LARSON, R.G. & FREDERICKSON, G.H. 1989 The stability of gravity driven viscoelastic film-flow at low to moderate Reynolds number. *J. Non-Newtonian Fluid Mech.* **31**, 87–113.

SHEMILT, J.D., HORSLEY, A., JENSEN, O.E., THOMPSON, A.B. & WHITFIELD, C.A. 2022 Surface-tension-driven evolution of a viscoplastic liquid coating the interior of a cylindrical tube. *J. Fluid Mech.* **944**, A22.

SHEMILT, J.D., HORSLEY, A., JENSEN, O.E., THOMPSON, A.B. & WHITFIELD, C.A. 2023 Surfactant amplifies yield-stress effects in the capillary instability of a film coating a tube. *J. Fluid Mech.* **971**, A24.

SMOLKA, L., NORTH, J. & GUERRA, B. 2008 Dynamics of free surface perturbations along an annular viscous film. *Phys. Rev.* E **77**, 036301.

YIH, C.-S. 1967 Instability due to viscosity stratification. *J. Fluid Mech.* **27** (2), 337–352.

ZHANG, Y.L., MATAR, O.K. & CRASTER, R.V. 2002 Surfactant spreading on a thin weakly viscoelastic film. *J. Non-Newtonian Fluid Mech.* **105**, 53–78.

ZHOU, Z.-Q., PENG, J., ZHANG, Y.-J. & ZHUGE, W.-L. 2014 Instabilities of viscoelastic liquid film coating tube in the presence of surfactant. *J. Non-Newtonian Fluid Mech.* **204**, 94–103.

ZHOU, Z.-Q., PENG, J., ZHANG, Y.-J. & ZHUGE, W.-L. 2016 Viscoelastic liquid film flowing down a flexible tube. *J. Fluid Mech.* **802**, 583–610.